Single-cell analysis of innate spinal cord regeneration identifies intersecting modes of neuronal repair

Vishnu Muraleedharan Saraswathy[1,2], Lili Zhou[1,2] and Mayssa H. Mokalled[1,2,3]

[1] Department of Developmental Biology
Washington University School of Medicine, St. Louis, MO, USA 63110.

[2] Center of Regenerative Medicine
Washington University School of Medicine, St. Louis, MO, USA 63110.

[3] Author for correspondence: mmokalled@wustl.edu

ABSTRACT

Adult zebrafish have an innate ability to regenerate spinal cord tissues within 6 to 8 weeks of injury. To achieve a comprehensive molecular understanding of neural repair mechanisms in zebrafish, we generated a single nuclear RNA sequencing atlas that spans 6 weeks of regeneration. Our dataset surveyed dynamic cellular and molecular changes after injury, and revealed neurons as signaling hubs across time points. Using *in silico* and *in vivo* analysis of neurotransmitter properties, we found that neurogenesis of excitatory and inhibitory neurons restores the excitatory/inhibitory balance during regeneration. In addition to balanced neurogenesis, one cluster of injury-responsive neurons (iNeurons) activates a regenerative transcriptional signature 1 to 3 weeks post-injury. Cross-species comparisons between zebrafish and mouse neurons uncovered transcriptional similarities between iNeurons and a rare population of spontaneously plastic neurons in mouse spinal lesions. Using CRISPR/Cas9 mutagenesis, we showed that iNeuron genes are required for spinal cord repair, and identified vesicular trafficking as an essential mechanism that underlies spontaneous plasticity in iNeurons. This study provides a comprehensive resource of the cells and mechanisms that direct spinal cord regeneration in zebrafish, and identifies cooperative roles for spontaneous neuronal plasticity and adult neurogenesis during innate spinal cord repair.

INTRODUCTION

Mammalian spinal cord injuries (SCI) elicit complex multi-cellular responses that impede regeneration and cause permanent functional deficits in mammals (He and Jin, 2016; Brennan and Popovich, 2018; Sofroniew, 2018; Milich et al., 2019; Fouad et al., 2021; Tran et al., 2022). Anti-regenerative neuron-extrinsic factors comprise chronic inflammation, fibrotic scarring, demyelination and the acquisition of a regeneration restricting extracellular milieu. These injury complications exacerbate the inherently limited ability of the mammalian spinal cord (SC) to replenish lost neurons via adult neurogenesis or to regrow lesioned axon tracts. Consequently, even the most groundbreaking regenerative therapies targeting select cell types or individual molecules have only yielded modest improvement in cellular and functional outcomes (Park et al., 2008; Sofroniew, 2018). SCI studies have since pursued combinatorial strategies as a more promising therapeutic avenue (DePaul et al., 2017; Anderson et al., 2018; Nakamura et al., 2021). We propose that comprehensive and simultaneous examination of neuronal and non-neuronal cells after SCI is fundamental to understanding and manipulating the multi-cellular complexities of neural injuries.

Unlike mammals, adult zebrafish have an innate ability to spontaneously recover from severe SCI. Following complete transection of SC tissues, zebrafish reverse paralysis and regain swim function within 6 to 8 weeks of injury (Mokalled et al., 2016; Burris et al., 2021). Pro-regenerative injury responses involving immune and progenitor cells, neurons and glia, cooperate to achieve spontaneous and efficient repair in zebrafish (Reimer et al., 2008; Kuscha et al., 2012; Briona et al., 2015; Cavone et al., 2021; Klatt Shaw et al., 2021; Vandestadt et al., 2021; Saraswathy et al., 2022). Early after SCI, potent populations of progenitor cells, including central canal-surrounding ependymo-radial glial cells (ERGs), are activated to replenish lost neurons and glia (Reimer et al., 2008; Briona et al., 2015; Klatt Shaw et al., 2021; Saraswathy et al., 2022). Newly differentiated motor neurons and interneurons populate the regenerate tissue, as pre-existing neurons regrow axons across lesioned tissues (Reimer et al., 2008; Kuscha et al., 2012; Saraswathy et al., 2022). Though less studied, glial cells are thought to enact instrumental pro-regenerative responses throughout the course of regeneration (Goldshmit et al., 2012; Mokalled et al., 2016; Klatt Shaw et al., 2021). Bridging glia extend cellular bridges across the lesion and oligodendrocytes direct remyelination, in addition to glial support of neuronal survival and functions. However, a holistic understanding of the cellular interactions that coordinate the pro-regenerative responses to direct SC regeneration in zebrafish is to be acquired.

The advent of single-cell transcriptomics provided the tools to achieve a refined understanding of molecular SCI responses across species and cell types. Multiple single-cell RNA sequencing (scRNA-seq) atlases have been generated for mouse SCI, rat SCI or human SC tissues (Milich et al., 2021; Matson et al., 2022; Yao et al., 2022; Rodrigo Albors et al., 2023; Yadav et al., 2023). Single-cell studies from mice revealed new insights into macroglial cell-cell interactions after injury, revealed a rare population of lumbar spinocerebellar neurons that elicit a regeneration signature, or characterized the responses of astrocytes after injury (Milich et al., 2021; Hou et al., 2022; Matson et al., 2022; Rodrigo Albors et al., 2023). However, single-cell studies from zebrafish SC tissues have been limited to isolated immune or progenitor motor neuron cells and to larval stages (Cavone et al., 2021; Scott et al., 2021). Thus, a complete resource of the regenerative cells and mechanisms from adult zebrafish is required to develop a molecular understanding of the cell identities that enable or limit spontaneous plasticity and regeneration.

The fundamental principles that determine or limit regenerative capacity across species have eluded scientists for ages. While pro-regenerative injury responses are overwhelmed by anti-regenerative complications in mammals, zebrafish cells exhibit increased potency and exclusively pro-regenerative signatures after SCI. Molecular and cellular studies of select cell types or regenerative pathways revealed key insights into the cellular contributions and molecular signatures associated with elevated regenerative capacity. Specifically, while ependymal cells elicit limited stem cell potential in adult mice (Ren et al., 2017; Shah et al., 2018), zebrafish ERGs retain radial glial features and contribute to neurogenesis and gliogenesis after SCI (Reimer et al., 2008; Briona et al., 2015; Klatt Shaw et al., 2021; Saraswathy et al., 2022). The disparities in neuron progenitor capacities between zebrafish and mammals yielded an assumption that neurogenesis-based neural repair is unachievable in mammals and directed the community's efforts toward plasticity-based neural repair strategies. However, while zebrafish has been an established model of neuron regeneration, it remains unclear whether zebrafish could contribute insights and applications into plasticity-driven repair mechanisms. Thus, how and why neuronal injury responses differ between zebrafish and mammals require comprehensive molecular investigation and cross-species comparisons.

This study presents an atlas of the dynamic responses across major spinal cell types during early, intermediate and late stages of regeneration in adult zebrafish. Single nuclear RNA sequencing (snRNA-seq) was performed at 0, 1, 3 and 6 weeks post-injury. Neurons elicit elevated signaling activity relative to the dozens of cell types that respond to injury. While SCI

disrupts the excitatory/inhibitory neuron balance, sequential neurogenesis of excitatory and inhibitory neurons restores the homeostatic neuronal landscape at late stages of regeneration. In addition to regenerating new neurons, a transient regenerative signature emerges in a population of injury-responsive neurons (iNeurons) between 1 and 3 weeks post-injury. iNeurons are transcriptionally analogous to a rare population of mouse neurons that show spontaneous plasticity after injury (Matson et al., 2022). iNeuron markers genes are required for functional SC repair, and dynamic vesicular trafficking is a central mechanism that promotes spontaneous neuronal plasticity. This study identifies multi-layered modes of regenerative neurogenesis and neuronal plasticity during innate spinal cord regeneration, and establishes zebrafish as a platform to identify and manipulate regeneration- and plasticity-based modes of neural repair.

RESULTS

Molecular identification and temporal dynamics of cell types during SC regeneration.

To determine the transcriptional identities of the cells that directs successful SC regeneration, we performed complete SC transections on adult zebrafish and dissected 3 mm sections of SC tissues surrounding the lesion site at 1, 3, and 6 weeks post-injury (wpi) for nuclear isolation. Corresponding tissue sections were collected from uninjured controls. SC tissues were pooled from 50 animals per time point, and 2 pools of independent biological replicates were analyzed for each time point. Our dataset spans key regenerative windows including early injury-induced signals at 1 wpi, neuronal and glial regeneration at 3 wpi, and cellular remodeling at late stages of regeneration at 6 wpi (Mokalled et al., 2016). Isolated nuclei were sequenced using 10x genomics platform (3' v3.1 chemistry) and a total of 73,814 nuclei were obtained (Matson et al., 2018). Nuclei were subsequently filtered to exclude droplets that included no nuclei or nuclei doublets before proceeding with downstream analysis using the Seurat package (Fig. 1A and S1A-C).

Clustering of SC nuclei revealed 41 cell clusters with distinct molecular identities and temporal dynamics (Fig. S1D). Postulating that previously established cell type classifiers are likely biased toward cell identities present the mammalian nervous system or in developing zebrafish, we optimized cell type identification by generating a custom-assembled Vertebrate CNS Marker (VNM) database. VNM compiled cell type markers commonly present in the central nervous system from over 12 datasets and vertebrate species including zebrafish, mice, and humans (Guillemot, 2007; Zhang et al., 2014; Lu et al., 2015; Hernandez-Miranda et al., 2017; Tang et al., 2017; Haring et al., 2018; Hayashi et al., 2018; Rosenberg et al., 2018; Sathyamurthy et al., 2018;

Zeisel et al., 2018; Baek et al., 2019; Rougeot et al., 2019; Tambalo et al., 2020; Cavone et al., 2021; Milich et al., 2021). We then cross-referenced the differentially expressed (DE) markers for each cluster with our VNM database (Table S1 and Fig. S1E). Scoring matrix heatmap from this analysis identified 8 major cell types comprising neurons, glia/ERGs, oligodendrocyte precursor cells (OPCs), oligodendrocytes, leukocytes, pericytes and endothelial cells, in addition to one cell cluster of undetermined identity (Fig. 1B and S1E). VNM-based cell type classification was further confirmed by evaluating the expression of canonical marker genes for each cluster (Fig. 1C). *elavl4* and *snap25a* were enriched in neurons, *gfap* and *slc4a10a* in glia/ERGs, *cspg4* and *sema5a* in OPCs, *mpz* and *mbpa* in oligodendrocytes, *lgals9l1* and *ptprc* in leukocytes, *col1a1b* and *col1a1a* in pericytes, and *igfr1b* and *col4a1* in endothelial cells (Fig. 1C). Although these canonical markers were enriched in their respective clusters, the proportions of cells expressing *lgals9l1* and *ptprc* in leukocytes, *col1a1b* and *col1a1b* in pericytes, and *igfr1b* and *col4a1* in endothelial cells were relatively small. We conclude that our VNM database is likely still biased toward commonly used mammalian cell markers that are not necessarily the best markers for adult zebrafish, and that our single-cell atlas provides a platform to identify improved CNS markers for adult zebrafish cells. To test this hypothesis, we examined whether our snRNA-seq dataset identified improved cell-specific DE markers in adult zebrafish SCs (Fig. 1F). Glia/ERG cells expressed the cilia-associated *cfap57* gene, indicative of the ciliated nature of the SC central canal-lining ERGs. Leukocytes were enriched for *mrc1b* and *slco2b1* genes along with the cell adhesion molecule coding *mcamb* gene. Finally, pericytes (expressing *ahnak, plpp3* and *ctgfb*) and endothelial cells (expressing *pxdn* and *bcam*) shared several DE markers including multiple collagen family genes such as *col4a1*. These studies indicated that extrapolating mammalian CNS or developmental zebrafish markers requires validation, and provided a platform to identify new and improved CNS cell markers in adult zebrafish.

To examine the temporal dynamics of SC cells during regeneration, we determined the numbers and relative proportions of nuclei within each coarse cluster in the integrated dataset (Fig. 1D-E and S1F-G). Neurons comprised 39% of the nuclei harvested from uninjured SCs, but their proportion decreased to 18% at 1 wpi and recovered to 27% at 6 wpi. Expectedly, the proportions of leukocytes increased from 11% of total nuclei prior to injury to 23% at 1 wpi and gradually decreased to 15% at 6 wpi. We observed an expansion in the relative abundance of glia/ERGs between 1 and 3 wpi, whereas OPCs maintained similar proportions at all timepoints. Pericytes and endothelial cells comprised 1.3% and 0.9% of uninjured nuclei, and their proportions increased to 1.7% and 2.3% of total nuclei at 1 wpi, respectively. These studies

provided a comprehensive resource of the cellular architecture that directs successful SC repair and revealed a gradual recovery in neuronal proportions during innate SC repair.

Neurons are active signaling hubs during spinal cord regeneration.

To infer molecular modes of intercellular communication during SC regeneration, we surveyed signaling pathways that are differentially active between 0 and 6 wpi (Fig. 2 and S2). We first converted our dataset of zebrafish genes to their human orthologues using the BioMart package from Ensembl. The CellChat R package was then used to quantitatively analyze global intercellular communication networks based on the expression of ligands, receptors and cofactors (Jin et al., 2021). In control SC tissues, the cumulative strengths of outgoing signaling pathways were highest in neurons and OPCs relative to other cell types, indicating active signaling in neurons and glia under homeostatic conditions (Fig. 2A-B). After SCI, the cumulative strengths of outgoing signaling increased in all cell types, indicating tissue-wide responses are activated after injury (Fig. 2A-B). The strengths of outgoing signaling pathways from endothelial cells and pericytes peaked at 1 wpi, whereas signaling from oligodendrocytes was highest at 6 wpi (Fig. 2A-B). These results are consistent with early activation of endothelial cells and pericytes after injury, and support a later role for oligodendrocytes during remyelination of regenerating axons. Notably, outgoing signaling from neurons was elevated across all time points and increased 2.5-fold between 0 and 6 wpi (Fig. 2A-B). Incoming signaling strengths received by neurons also increased 2.5-fold between 0 and 6 wpi (Fig. S2A-B). Incoming signaling received by OPCs was highest among spinal cell types across all time points (Fig. S2A-B). Confirming our CellChat analysis, trajectory inference analysis showed OPCs and neurons, along with glia/ERGs and oligodendrocytes, have elevated transcriptional activity during SC regeneration (Gulati et al., 2020) (Fig. S2C). Mapping of ligand-receptor interactions predicted cell-cell signaling interactions are highest between neurons and OPCs (Fig. 2C). These results indicated neurons and OPCs have elevated and dynamic transcriptional and signaling activities during zebrafish SC regeneration.

Global and neuron-specific analyses of injury-induced signaling pathways.

Global CellChat analysis revealed 25 to 29 active signaling pathways in control, 3 and 6 wpi SC tissues. The highest number of signaling pathways (35 pathways) were enriched at 1 wpi, indicating abundant and dynamic intercellular communication during early stages of SC regeneration (Fig. 2D). Overall, 13 pathways were enriched at 1, 3 or 6 wpi relative to uninjured controls, and 5 of the 13 injury-induced pathways were specifically induced at 1 wpi. Globally-

induced signaling pathways included cell adhesion signaling networks (L1CAM, JAM3, CNTN1 and EPHA2/3/4/5), extracellular matrix (ECM) mediated signaling networks (TENASCIN, PDGFB, FN1, MDK, SEMA3A/B/C, ENTPD1 and HSPG2) and developmental signaling pathways (BMP7 and NOTCH1/2/4) (Fig. 2D).

To identify molecular pathways that account for elevated neuron signaling, we focused our subsequent analysis on signaling pathways predicted to be outgoing from or incoming into neurons (Fig. 2E and S2D). For outgoing signaling, 17 to 22 pathways were predicted to be activated by neurons between 0 and 6 wpi. In addition to homeostatic signaling pathways increasing in strengths after injury, 6 pathways were injury-induced and 4 out of the 6 injury-induced pathways were specific to 1 wpi neurons (Fig. 2E-F). Cell adhesion molecules mediate the cell-cell and cell-ECM interactions necessary for cell survival, migration, synaptogenesis and axon guidance during regeneration (Walsh and Doherty, 1996; Zhang et al., 2008). Specifically, the L1 cell adhesion molecules (L1CAM) are members of the immunoglobulin superfamily of cell adhesion molecules that were previously shown to be upregulated in axons after CNS injury (Bernhardt et al., 1996; Jung et al., 1997; Zhang et al., 2008). We found that L1CAM signaling is highly active in neurons and glial cells, suggesting L1CAM plays neuronal and axon-independent regenerative roles (Fig. 2F). Ephrin A (EPHA) signaling, which is best studied for its role in cell adhesion, positioning and migration, is activated between neurons, OPCs and pericytes after injury (Fig. 2F). The cell adhesion molecule Contactin-1 (CNTN-1) interacts with NRCAM (data not shown), mediating signaling crosstalk between neurons, glia/ERGs and endothelial cells (Haenisch et al., 2005; Mikami et al., 2009) (Fig. 2F). By providing either permissive or non-permissive microenvironments after injury, growth factors and ECM components play crucial regenerative roles after SCI. Tenascins are matricellular proteins that modulate cell adhesion, migration and growth (Busch and Silver, 2007). We found TENASCIN signaling, mediated by TENASCIN-R (TNR) and the integrins ITGAV and ITGB6 (data not shown), is a major neuron- and OPC-derived pathway that converges onto endothelial cells after SCI (Fig. 2F). These studies revealed complex multicellular communication networks that coordinate signaling between neurons, glia non-neural injury-responding cells during SC repair.

Neuronal E/I balance is restored during successful SC regeneration.

To explore the cellular dynamics that support neuronal and functional recovery after zebrafish SCI, we examined neuronal cell types and states prior to and after injury. Subcluster analysis identified 30 distinct neuron clusters between 0 and 6 wpi (Fig. 3A and S3A-B). Balanced synaptic

excitatory and inhibitory (E/I) transmission is a central feature of CNS function as altered E/I balance results in severe behavioral defects in humans (Isaacson and Scanziani, 2011). Despite eliciting features of cellular regeneration, SCI in mouse neonates causes impaired locomotor recovery due to imbalanced E/I transmission (Dudek and Sutula, 2007; Gao and Penzes, 2015; Bertels et al., 2022). With zebrafish recovering swim function after SCI, we postulated that balanced E/I transmission is a feature of functional SC repair in zebrafish. To test this hypothesis, we first performed a bioinformatic characterization of the excitatory and inhibitory neurotransmitter properties of the neuron clusters identified in our dataset (Fig. 3B). Neuron classification was based on the expression of classical markers of excitatory (slc*17a6a, slc17a6b*), inhibitory (*slc6a5, gad1a, gad1b, gad2*) and cholinergic (*chata, slc5a7a*) neurons (Fig. S4C). Neuron subclusters were classified as excitatory, inhibitory, cholinergic, excitatory/cholinergic, and inhibitory/cholinergic (Fig. 3B and S3C-E). The proportions of excitatory (13.9%) was lower than inhibitory (36.1%) neurons in uninjured SC tissues (Fig. 3C), resulting in a baseline E/I ratio of 0.4 (Fig. 3D). The profile of excitatory neurons rapidly increased to 21.1% of total neurons at 1 wpi and stabilized at 21.6% at 2 wpi (Fig. 3C). Inhibitory neurons accounted for 48.6% of total neurons at 1 wpi and continued to expand to 59.4% at 2 wpi (Fig. 3C). By 6 wpi, the relative proportions of excitatory and inhibitory neurons returned to near baseline levels, accounting for 16 and 42.2% of total neurons, respectively (Fig. 3C). Bioinformatic calculation of the E/I ratio confirmed an imbalance toward an excitatory phenotype at 1 wpi and a recovery to baseline levels by 6 wpi (Fig. 3D).

To validate our bioinformatic E/I balance calculations *in vivo*, we generated dual transgenic reporter fish that simultaneously label glutamatergic excitatory neurons (*vglut2a*:RFP) and GABAergic inhibitory neurons (*gad1b*:GFP) (Satou et al., 2013). Complete SC transections were performed on double transgenic animals and SC tissues were collected for histological examination at 0, 1, 3 and 6 wpi (Fig. 3E-F). Absolute numbers and relative proportions of RFP-, GFP- and HuC/D-expressing neurons were quantified in SC cross sections at 450 μm rostral to the lesion as a proxy evaluation of the E/I landscape during regeneration. Compared to control SC tissues, the profiles of *vglut2a* $^{+}$ excitatory neurons (*vglut2a* $^{+}$ HuC/D^{+}) showed doubled in proportion at 1 wpi and were maintained near 1 wpi levels until 6 wpi (Fig. 3G and S3F). On the other hand, the profiles of *gad1b*$^{+}$ inhibitory neurons (*gad1b*$^{+}$ HuC/D^{+}) gradually increased by between 1 and 6 wpi relative to controls (Fig. 3H and S3G). Notably, the absolute numbers of HuC/D^{+} neurons drastically increased at 1 and 3 wpi, indicating extensive neuronal remodeling during SC regeneration (Fig. S3H). Thus, consistent with our snRNA-seq findings, these *in vivo*

studies confirmed an early surge in excitatory neurons at 1 wpi and a recovery of the E/I balance toward baseline levels by 6 wpi (Fig. 3I).

Neurogenesis of excitatory and inhibitory neurons after SCI.

We next explored the cellular bases behind the recovery of E/I balance during zebrafish SC repair. The observed E/I ratio changes could be due to sequential neurogenesis of excitatory then inhibitory neurons after SCI. Alternatively, E/I ratios could reflect plasticity and changes in the neurotransmitter properties of pre-existing neurons. To distinguish between these possibilities, we first performed a cell proliferation assay. Dual transgenic fish for *vglut2a*:RFP and *gad1b*:GFP were subjected to SCI and a single EdU pulse for 24 hrs prior to SC tissue collection. SC tissues were harvested at 1, 3 and 6 wpi for co-labelling with the proliferation marker EdU (Fig. 4A-B and S4A). SC tissues from uninjured animals that received a single EdU injection for 24 hrs were harvested as controls. In striking manifestation of the regenerative capacity of zebrafish SC tissues after SCI, EdU incorporation was markedly elevated at 1 wpi relative to 0, 3, and 6 wpi (Fig. 4C and S4B). The profiles and absolute numbers of newly generated glutamatergic neurons (*vglut2a*$^+$ EdU$^+$) peaked at 1 wpi relative to control, 3 or 6 wpi SC sections (Fig. 4D and S4C), supporting a surge of regenerating excitatory neurons at 1 wpi. As the profiles of GABAergic neurons showed a gradual increase up to 6 wpi (Fig. 3H) and due to low numbers of EdU$^+$ cells at 3 and 6 wpi, we were unable to evaluate the profiles of newly generated GABAergic neurons with a single EdU pulse (Fig. 4E and S4D).

To overcome this limitation and evaluate the numbers of regenerating glutamatergic and GABAergic neurons after SCI, we performed SC transections on *vglut2a*:RFP and *gad1b*:GFP dual transgenic fish followed by daily EdU injections for 1 or 3 wpi (Fig. 4F-G and S4E). Uninjured control animals received daily EdU injections for 1 week prior to SC tissue collection. Compared to single EdU pulses, daily EdU labeling allowed us to estimate the total and cumulative profiles of regenerating neurons. To account for anatomical differences along the proximo-distal axis of lesioned SC tissues, RFP-, GFP- and EdU-expressing cells were quantified from SC sections 150, 450 and 750 μm rostral to the lesion. The numbers and proportions of EdU$^+$ cells sharply increased at 1 wpi and showed less pronounced additive EdU incorporation at 3 wpi (Fig. S4F-G). The profiles of newly formed glutamatergic (EdU$^+$ *vglut2a*$^+$) neurons markedly increased at 1 and 3 wpi relative to controls (Fig. 4H and S4H). The profiles of regenerating GABAergic (EdU$^+$ *gad1b*$^+$) neurons were significantly elevated at 1 wpi compared to controls, and continued to increase at 3 wpi compared to 1 wpi (Fig. 4I and S4I). As proximal tissue sections (150 μm from

lesion) showed elevated neurogenesis across time points, differential dynamics of glutamatergic and GABergic neuron regeneration were most prominent in more distal SC sections (750 μm from lesion) (Fig. 4H and 4I). At these levels, the profiles of newly formed glutamatergic (EdU$^+$ *vglut2a*$^+$) neurons sharply increased at 1 wpi and maintained comparable presence at 3 wpi (Fig. 4H), whereas GABAergic (EdU$^+$ *gad1b*$^+$) continuously increased from 1 to 3 wpi (Fig. 4I). Together, these *in vivo* studies showed glutamatergic neurogenesis precedes a continuous and slower regeneration timeline for GABAergic neurons, suggesting that sequential neurogenesis of different neuron subtypes around the lesion accounts for the dynamic changes in E/I properties during zebrafish SC regeneration.

Identification of injury-responsive iNeurons during SC regeneration.

To delve into the distribution of specific neuron subclusters prior to and after SCI, we calculated the numbers and relative proportions of each neuron subcluster between 0 and 6 wpi (Fig. 3A and S3A-B). Out of the 30 neuron types subclustered from our integrated dataset, 2 subclusters (neuron subclusters N18 and N22) were exclusively present after injury and are referred to hereafter as injury-responsive neurons or iNeurons (Fig. 5A and S5A). Our analysis retrieved equal numbers of N18 and N22 iNeurons at 1 wpi (Fig. 5A). The number and proportion of N18 iNeurons gradually decreased between 1 and 6 wpi. Conversely, N22 iNeurons were sharply depleted by 85% at 3 wpi and not detectable at 6 wpi (Fig. 5A). DE marker analysis identified *ebf2, gdf11, lhx4* and *kidins220a* as N18 iNeuron markers but failed to determine a clear transcriptional signature that distinguishes N18 iNeurons from other neuron clusters (Fig. 5B). On the other hand, in support of a pro-regenerative role for N22 iNeurons, *atf3* and *sox11b* were specifically enriched in N22 iNeurons (Fig. 5C). *atf3* and *sox11b* are known markers and drivers of neuronal survival and axon regrowth in zebrafish and mice (Jankowski et al., 2009; Jing et al., 2012; Wang et al., 2015; Gey et al., 2016; Wang et al., 2017; Kole et al., 2020). By gene ontology (GO) analysis, functional terms associated with axon development and regrowth, synaptic activity and vesicular trafficking were highly enriched in N22 iNeurons (Fig. 5D). These findings indicated N22 iNeurons comprise a transient subpopulation of injury-responsive neurons that contributes to functional SC repair.

iNeurons are signaling hubs during SC regeneration.

To evaluate the role of N22 iNeurons during SC regeneration, we determined the extent and identities of the signaling pathways that are initiated and received by N22 iNeurons using CellChat. To specifically identify N22 iNeurons within the rest of the SC microenvironment, we

first tracked and identified N22 iNeurons in the integrated dataset that includes all SC cells (Fig. S5A). Clusters 5 and 21 from the integrated dataset accounted for the majority of N22 iNeurons and were renamed iNeurons for CellChat analysis (Fig. S5B). Strikingly, compared to the global cell-interactions derived from the integrated dataset (Fig. 5E), the cumulative and reciprocal signaling strengths were highest between iNeurons and OPCs at 1 wpi (Fig. 5F). The cumulative strengths of outgoing and incoming signaling were markedly lower in the rest of the neuronal cells compared to iNeurons (Fig. 5F and S5C).

To examine the molecular features of the crosstalk between iNeurons and OPCs, we identified major signaling networks that are either incoming or outgoing from iNeurons (Fig. 5F and S5D). CellChat analysis showed iNeurons have a high probability to transduce SEMA5 and NRXN3 signaling into OPCs and other neurons, respectively (Fig. 5F). NRX3, CDH4 and CADM1 signaling were also identified as highly probably incoming and outgoing iNeuron signals (Fig. 5F and S5D). Consistent with the gene ontology of N22 iNeuron genes (Fig. 5B), we observed a high probability for reciprocal Neuregulin (NRG)-ERBB signaling between iNeurons and OPCs at 1 wpi (Fig. 5F and S5D). ErbB signaling was recently shown to regulate OPC transformation and spontaneous remyelination after SCI in mice (Bartus et al., 2019). We found NRG2 and NRG3 ligands expressed by OPCs are the most probable activators of the ERBB4 receptor expressed in iNeurons (Fig. 5F). Reciprocally, there are several interaction probabilities for the NRG1/2/3 and ERBB2/4 as outgoing signaling ligands from iNeurons to OPCs (Fig. S5D). These results showed iNeurons are potent centers of molecular signaling during SC regeneration, and suggested that reciprocal signaling between iNeurons and OPCs is a central feature of innate SC repair.

Cross-species comparisons between zebrafish and mouse neurons.

To explore potential similarities and differences between zebrafish and mouse neurons after SCI, we integrated our neuronal snRNA-seq data with a recently published dataset that dissected the transcriptional identities of mouse neurons after SCI (Matson et al., 2022). Notably, Matson *et al.* identified a rare population of mouse SC neurons that express regeneration associated genes (RAG) after injury and that are referred to hereafter as RAG neurons (or *Mm*_RAG neurons) (Matson et al., 2022). Gene expression in the RAG cluster included *Atf3* and *Sox11*, suggesting mouse RAG neurons and zebrafish iNeurons may have similar transcriptional profiles. To integrate the transcriptomic datasets for mouse SCI (Gene Expression Omnibus GSE172167) with our zebrafish snRNA-seq dataset, we first converted our zebrafish genes to their mouse

orthologues using BioMart of Ensemble, then identified neuronal cell populations from both datasets before proceeding with cross-species integration. Subclustering of integrated mouse and zebrafish neurons revealed 45 different clusters (referred to hereafter as ZM clusters) with different dynamic distributions across timepoints and species (Fig. 6A-B and S6). UMAP plot and cell numbers across all time points showed that 46.6% of neuronal ZM clusters were overwhelmingly populated by both mouse and zebrafish neurons (at least 50 cells from each species) (Fig. 6B and S6A). 28.9% of ZM clusters comprised fish-only clusters (ZM3, 10, 17, 28, 30, 31, 32, 34, 37, 39, 40, 43 and 44), with 24.4% of ZM clusters including mouse-only clusters (ZM6, 9, 16, 26, 27, 33, 35, 36, 38, 41 and 42). These studies underscored differences and similarities between the transcriptional landscapes of zebrafish and mouse neurons after SCI.

To identify zebrafish iNeurons and mouse RAG cells within the integrated ZM dataset, we examined the expression of top iNeuron and RAG DE markers in the integrated dataset. *atf3, sox11, gap43, vamp4, syt11, hdac10* and *mthfd1l* were used for zebrafish iNeuron classification. *Atf3, Sox11, Gap43, Sprrr1a, Tnfrs12a, Klf6, Bdnf* and *Adcyap1* were used for mouse RAG identification. Markers that are common to both iNeurons and RAG cluster (*atf3*, *sox11* and *gap43*) were enriched in cluster ZM20 (Fig. 6C-E). RAG cluster markers (*Tnfrsf12a, Bdnf, Klf6* and *Adcyap1*) and iNeuron markers (*Vamp4, Hdac10, and Mthfd1l*) were also enriched in cluster ZM20 (Fig. 6C). By tracing the identities of zebrafish iNeurons within our integrated ZM dataset, 50% of zebrafish iNeurons mapped to cluster ZM20 (Fig. 6D). The numbers of proportions of ZM20 cells peaked at 1 wpi in zebrafish and between 1 and 3 wpi in mice (Fig. 6E and S6B). Mapping iNeuron and RAG cells within cluster ZM20 showed these two populations were adjacently situated in the UMAP plot and did not split into separate clusters at higher resolution, indicating their transcriptional similarity (Fig. 6F). DE marker comparisons verified the transcriptional similarities between N18 iNeurons, N22 iNeurons and mouse RAG neuron markers (Fig. 6G). Gene ontology analysis showed that zebrafish iNeurons and mouse RAG clusters are significantly enriched with shared pro-regenerative GO terms including axon guidance, synapse organization and vesicular trafficking (Fig. 6H). These findings indicated that zebrafish iNeurons and mouse RAG neurons clustered into the ZM20 cluster following cross-species data integration, and suggested zebrafish iNeurons and mouse RAG cells share transcriptional and functional similarities.

***in vivo* mapping of iNeurons during SC regeneration.**

To validate the emergence of an iNeuron transcriptional signature in regenerating SC tissues, we performed HCR *in situ* hybridization for select markers that are uniquely expressed in N22 iNeurons and compared to all other spinal types in the integrated dataset (Fig. 5C). To enable differential labeling of regenerating and pre-existing neurons, wild-type fish were subjected to SCI and daily EdU injections. *syt11b* and *vamp4* HCR *in situ* hybridization and staining for HuC/D and EdU were performed at 0, 1 and 3 wpi (Fig. 7A and 7D). To test whether iNeuron markers are preferentially expressed in neurons, integrated densities of their HCR *in situ* hybridization signals were quantified in total SC tissues and in HuC/D$^+$ neurons (Fig. 7A-F and S7A-H). At 1 wpi, *synaptotagmin XI b (syt11b)* expression increased by 3.6-fold in total SC tissues and by 4.3-fold in HuC/D$^+$ neurons (Fig. 7B-C). *syt11b* expression was reduced to its wild-type level by 3 wpi (Fig. 7B-C). Expression of vesicle-*associated membrane protein 4 (vamp4)* was upregulated at 1 and 3 wpi, with 2.3- to 2.5-fold increase in total SC tissues and HuC/D$^+$ neurons at 1 wpi (Fig. 7E-F). Since *syt11b* showed robust expression and upregulation in neurons and to address putative redundancy between the *syt11b* and *syt11a* paralogs, we examined *syt11a* expression after SCI (Fig. S7A-E). Like *syt11b*, *syt11a* transcripts were upregulated after injury, including in neurons. However, unlike *syt11b*, *syt11a* expression was not restricted to neurons including expression in ependymal cells surrounding the central canal at 1 wpi (Fig. S7E). These findings validated *syt11b* and *vamp4* as markers of zebrafish iNeurons during spinal cord regeneration.

iNeurons are surviving neurons that elicit spontaneous plasticity after injury.

The emergence of an iNeuron transcriptional profile at 1 wpi raised a central question related to the origin of their pro-regenerative signature. We postulated that iNeurons could either represent newly formed regenerating, or a population of spontaneously plastic neurons that survive injury and support immediate repair. To distinguish between these hypotheses, we quantified the profiles of iNeurons that express *syt11b/a*, HuC/D and EdU (Fig. 7G-I and S7A-H). In these experiments, HuC/D$^+$ EdU$^+$ represent regenerating neurons and HuC/D$^+$ EdU$^-$ represent pre-existing neurons. Expectedly, the profiles of regenerating neurons significantly increased form 1 to 3 wpi, indicating potent neurogenic responses are activated during innate SC repair (Fig. 7H). At 1 wpi, *syt11b* transcripts labeled 14.5% of HuC/D$^+$ neurons (Fig. 7G), and only 6.4% of regenerating neurons (Fig. 7I). Even though *syt11a* labels slightly higher proportion of neurons (21.85%) at 1 wpi, more than 90% of the newly generated neurons don't show expression of *syt11a* (Fig. S7C-E). These results indicated that over 90% of iNeurons are pre-existing neurons that survive SCI.

Since the majority of iNeurons are pre-existing in control SC tissues, we examined whether iNeurons represent a specific population of neurons with elevated survival capacity or spontaneous plasticity. To address this question, we performed *syt11b* HCR *in situ* hybridization on *vglut2a*:RFP and *gad1b*:GFP dual transgenic fish, which label glutamatergic excitatory and GABAergic inhibitory neurons, respectively (Fig. 7J). Neuron subtypes not labeled with *vglut2a*:RFP or *gad1b*:GFP were labeled as others. The integrated density of *syt11b* transcript signals broadly increased at 1 wpi (Fig. S7I), including upregulated expression in *vglut2a*$^{+}$ and *gad1b*$^{+}$ neurons at 1 wpi (Fig. S7J-K). Notably, only 37.5% and 20.7% of the combined *syt11b* signal was found in glutamatergic and GABAergic neurons at 1 and 2 wpi, respectively, indicating that "other" neuron subtypes express the majority of *syt11b* during regeneration (Fig. 7K). These findings indicated that iNeurons do not represent a specific neuron subtype, and suggested that multiple zebrafish neurons survive SCI and elicit an iNeuron transcriptional and regenerative signature during early stages of SC repair.

iNeurons marker genes are required for cellular and functional recovery after SCI.

To evaluate the roles of iNeuron marker genes during SC regeneration, we employed CRISPR/Cas9 mutagenesis, SCI and functional swim assays (Fig. 8A) (Burris et al., 2021; Klatt Shaw and Mokalled, 2021). Among the top DE markers of N22 iNeurons, 10 genes were filtered as iNeuron-specific and chosen for mutagenesis (*hdac10, mthfd1l, si:ch211-153j24.3, fhdc5, shootin3, syt11b, fam171b, chrnb2b, fblim1, vamp4*) (Fig. 5C). *atf3* was selected as a positive control (Wang et al., 2017). In addition to targeting *syt11b*, we individually and combinatorially targeted the *syt11a* and *syt11b* paralogs to account for putatively redundant effects on regeneration. For efficient and simultaneous gene targeting in zebrafish, we used a recently adapted CRISPR/Cas9 protocol that achieves near complete mutagenesis in F0 injected adults (Burris et al., 2021; Klatt Shaw and Mokalled, 2021). CRISPR/Cas9 targeted animals (crispants) were raised to adulthood and mutagenesis rates were examined by capillary electrophoresis (Fig. S8A). Adult crispants with >90% mutagenesis were subjected to SCI, and swam against increasing water current inside an enclosed swim tunnel to screen for functional regeneration defects. At 4 wpi, swim endurance was significantly reduced in *atf3* and *vamp4* crispants (Fig. 8B). Targeting *syt11a and syt11b* paralogs individually did not alter swim endurance. However, swim endurance was diminished in *syt11a;syt11b* dual crispants, indicating the *syt11* paralogs were functionally redundant during SC repair (Fig. 8B). To validate swim capacity defects in iNeuron gene crispants, we tracked the swim behavior of *atf3*, *vamp4* and *syt11a;syt11b* crispants under at 0, 10 and 20 10 cm/sec current velocities (Fig. 8C). Compared to uninjected control

siblings and in the absence of water flow, swim distance was 50-55% reduced in *atf3* and *syt11a;syt11b* crispants and 25% reduced in *vamp4* crispants (Fig. 8C). Swim distance was significantly lower in *atf3*, *vamp4* and *syt11a/b* at 10 and 20 cm/sec water current velocities (Fig. 8C). These results indicated the iNeuron markers *atf3*, *vamp4* and *syt11a/b* are required for functional SC repair in zebrafish.

To date, cellular growth across the lesion has served as a primary readout of cellular regeneration in zebrafish. Glial bridging and axon tracing assays were performed to evaluate the extents of glial and axonal regeneration in iNeuron gene crispants. By Gfap immunostaining, the cross-sectional area of glial bridges was 65% reduced in *atf3* cripants at 4 wpi, but was unaffected in *vamp4* and *syt11a;syt11b* crispants compared to controls (Fig. 8D-E). At this time point, anterograde axon tracing using Biocytin showed comparable axon regrowth from hindbrain neurons into the proximal and distal SC sections between *vamp4*, *syt11a;syt11b* and control animals (Fig. 8F-G). Consistent with their defective glial bridging, axon regrowth into the proximal and distal sections of caudal SC tissues was markedly impaired in *atf3* cripants. Thus, *vamp4* and *syt11a/b* are required for functional SC repair but dispensable for cellular regeneration across the lesion. These studies showed iNeurons play essential regeneration-independent plasticity-based roles after SCI, and indicated vesicular trafficking is required for the recovery of local neuronal circuitry during innate SC repair.

DISCUSSION

This study presents a single-cell atlas of innate SC repair in adult zebrafish, uncovers neurons as potent signaling hubs after SCI, identifies cooperative modes of regeneration- and plasticity-based neuronal repair, and shows essential roles for vesicular trafficking in spontaneous neuronal plasticity.

The single-cell dataset generated in this study offers a comprehensive resource to determine regenerative cell identities and mechanisms in highly regenerative vertebrates. The use of snRNA-seq is ideal to profile the majority of spinal cell types in zebrafish. Single-cell RNA sequencing is inherently biased against larger cell types such as neurons and astrocytes (Lake et al., 2017; Bakken et al., 2018; Wu et al., 2019). snRNA-seq reduces the challenges of cell dissociation, retrieving large numbers of neurons and glia. While dissection- and dissociation-induced gene expression changes in control samples present a longstanding difficulty for tissue regeneration studies, our protocol minimizes background activation of injury-induced genes by

flash-freezing SC tissues from individual animals during tissue collection. Finally, large numbers of nuclei were obtained by pooling frozen SC tissues, minimizing confounding problems associated with snRNA-seq and allowing us to identify small cell populations (Lacar et al., 2016; Lake et al., 2017; van den Brink et al., 2017; Bakken et al., 2018; Ding et al., 2020). Overall, this dataset faithfully represents the proportions and dynamics of major cell populations during zebrafish SC regeneration.

Candidate approaches have unveiled central roles for several signaling pathways during SC regeneration (Reimer et al., 2009; Dias et al., 2012; Goldshmit et al., 2012; Zhang et al., 2018; Cavone et al., 2021). Yet, an integrated assessment of regenerative signaling pathways and global assessment of cell-cell interactions were missing. Using CellChat analysis, our single-cell dataset identified a myriad of cell-specific and injury-induced signaling pathways (Jin et al., 2021). Notably, comprehensive assessment of cell-cell signaling networks uncovered neurons as potent sources of signaling in homeostatic and lesioned SC tissues. Injury-induced neuronal signaling pathways include promoters of axon regrowth, survival, and migration such as L1CAM and CNTN (Walsh and Doherty, 1996; Zhang et al., 2008; Zhu et al., 2015). Equally enriched in neurons were repellent guidance molecules such as TENASCIN-R, SEMA3B and SEMA3C, enabling proper axon guidance and synapse targeting (Cohen et al., 2001; Becker et al., 2004; Falk et al., 2005; Ferrario et al., 2012). Further studies of injury-induced signaling pathways will shed light into signaling pathways that direct regeneration- or plasticity-driven SC repair.

SC tissues in adult zebrafish retain potent progenitor cells with radial glial features and established contribution to neurogenesis after SCI (Reimer et al., 2008; Briona et al., 2015; Saraswathy et al., 2022). SC regeneration is marked by early imbalance and late restoration of baseline E/I activity. Our data support a model in which excitatory neurons expand and repopulate regenerate SC tissues, while slower and continued neurogenesis of inhibitory neurons underlie the recovery of E/I balance at 6 wpi. These findings are consistent with published studies using a two-cut SCI model in adult zebrafish (Huang et al., 2021), and with the observation that *gad1b*:GFP and *vglut2a*:RFP expression domains are mutually exclusive in our SC sections. Genetic lineage tracing showed excitatory to inhibitory neurotransmitter switching has adverse effects on functional recovery after adult mouse SCI (Bertels et al., 2022). In zebrafish, fast motor neurons were shown to upregulate glutamate expression after injury or exercise (Bertuzzi et al., 2018). Although we cannot rule out similar mechanisms taking place in zebrafish, we found that a steady increase in the profiles of newly generated excitatory and inhibitory neurons account for

the recovery of E/I balance after SCI. We propose that in depth molecular evaluation of spinal progenitors is needed to better understand the potency and neurogenic capacities of neuronal progenitors during SC regeneration.

While zebrafish is an established model of neuron regeneration, our study establishes zebrafish as a renewed model to understand and manipulate fundamental mechanisms of plasticity-based neuronal repair. Neurogenesis-based neural repair is thought to be unattainable in mammals. Instead, the mammalian SCI field has directed its efforts to develop plasticity-based repair strategies. We propose that pre-existing zebrafish neurons upregulate an iNeuron transcriptional signature that includes regeneration associated genes, and that iNeurons elicit spontaneous plasticity during early stages of SC repair. The emergence of iNeurons after SCI is consistent with a recently identified population of embryonically derived dormant neurons that immediately respond to SCI in larval and adult zebrafish (Vandestadt et al., 2021). Similarity to the dormant precursor neurons reported by Vandestadt *et al.,* more than 90% of iNeurons are non-regenerating. At 1 wpi, iNeuron signaling accounts for the majority of total neuronal signaling, eliciting particularly strong interactions with OPCs. Intriguingly, cross-species transcriptomics highlighted transcriptional similarities between iNeurons and a rare population of spontaneously plastic spinocerebellar neurons (Matson et al., 2022). We propose that future zebrafish studies will contribute insights and applications into mechanisms of plasticity-driven neural repair.

Unbiased characterization of the molecular players that direct iNeuron functions after SCI showed multiple components of vesicular trafficking are required for functional SC repair in zebrafish. Syt11a/b (synaptotagmin XI a/b) and Vamp4 (vesicle-associate membrane protein 4) are vesicle-associated proteins that play different roles in neuronal synapses. Syt11 is a non-canonical SNARE that inhibits spontaneous neurotransmission and bulk endocytosis, whereas Vamp4 promotes Calcium-dependent excitatory neurotransmission release and bulk endocytosis (Nicholson-Fish et al., 2015; Wang et al., 2016; Shimojo et al., 2019; Lin et al., 2020; Bakr et al., 2021; Li et al., 2021). Our CRISPR/Cas9 studies showed *syt11a/b* and *vamp4* are required for the recovery of swim function after SCI in zebrafish. These findings are consistent with recent mammalian studies showing that inhibition of the presynaptic release machinery is important for axon regrowth (Hilton et al., 2022), and that *Syt11* knockout in excitatory forebrain neurons impairs synaptic plasticity and memory (Shimojo et al., 2019). Our data reveals vesicular trafficking is an essential mechanism that underlies spontaneous plasticity and rapid neurite outgrowth in iNeurons. We propose that zebrafish provide a valuable model to investigate the

origin of iNeurons, elucidate the role of vesicular trafficking in spontaneous plasticity, and identify new manipulations to promote plasticity after SCI.

ACKNOWLEDGMENTS

We thank S. Ackerman, V. Cavalli and A. Johnson for discussion and the Washington University Zebrafish Shared Resource for animal care. This research was supported by grants from the NIH (R01 NS113915 to M.H.M.) and a Postdoctoral Fellow Seed of Independence Grant from the Department of Developmental Biology at Washington University School of Medicine (to V.M.S.).

MATERIAL AND METHODS

Zebrafish

Adult zebrafish of the Ekkwill, Tubingen and AB strains were maintained at the Washington University Zebrafish Core Facility. All animal experiments were performed in compliance with institutional animal protocols. Size matched (~2 cm) male and female animals of ~4 months of age were used. SC transection surgeries and regeneration analyses were performed in a blinded manner. For all experiments, 2 to 4 independent experimental replicates were performed using different clutches of animals. Within each experiment, experimental fish and control siblings of similar size and equal sex distribution were used. Transected animals from control and experimental groups were housed in equal numbers (4-7 fish) in 1.1-liter tanks. The following previously published zebrafish trains were used: Tg(*vglut2a*:RFP) and Tg(*gad1b*:GFP) (Satou et al., 2013).

Spinal cord transection

Complete SC transections were performed as previously described (Mokalled et al., 2016). Briefly, zebrafish were anaesthetized in 0.2 g/L of MS-222 buffered to pH 7.0. Fine scissors were used to make a small incision that transects the SC 4 mm caudal to the brainstem region. Complete transection of the SC was visually confirmed at the time of surgery. Injured animals were also assessed at 2 or 3 dpi to confirm loss of swim capacity post-surgery.

Isolation of spinal cord nuclei from adult zebrafish

For nuclear isolation, a previously described method to isolate nuclei from mouse SC tissues was adapted to zebrafish SCs (Matson et al., 2018). Three mm SC tissue, flanking the lesion site were collected from 50 adult zebrafish at timepoints 1, 3 and 6 wpi. Corresponding segments of 3 mm SC tissue were collected from uninjured control animals. For tissue lysis, the detergent mechanical lysis protocol described by Matson et al. was performed. SC tissues were homogenized at low setting for 15 seconds. Density gradient separation using sucrose solution was used to sediment the nuclei from the supernatant. Final nuclear lysates were resuspended using 100 µl of resuspension solution (1x PBS + 2% BSA + 0.2U/µl RNase inhibitor - New England Biolabs, Cat#: M0314S). Hoechst staining was performed to assess the quality of isolated nuclei based on their shape. Samples in which more than 70% of the nuclei were scored as ‘healthy’ and submitted for single nuclear RNA sequencing.

Single nuclear RNA sequencing

For snRNA-seq, 30 µl of resuspension solution containing isolated nuclei at a concentration of ~1000 nuclei/µl was submitted to Genome Technology Access Center at McDonnel Genome Institute of Washington University. Two biological replicates of each timepoints at 0, 1, 3 and 6 wpi were used. cDNA was prepared after the GEM generation and barcoding, followed by the GEM-RT reaction and bead cleanup steps. cDNA was amplified for 11-13 cycles then purified using SPRIselect beads. Purified cDNA samples were then run on a Bioanalyzer to determine the cDNA concentration. GEX libraries were prepared as recommended by the 10x Genomics Chromium Single Cell 3' Reagent Kits User Guide (v3.1 Chemistry Dual Index) with appropriate modifications to the PCR cycles based on the calculated cDNA concentration. For sample preparation on the 10x Genomics platform, the Chromium Next GEM Single Cell 3' Kit v3.1, 16 rxns (PN-1000268), Chromium Next GEM Chip G Single Cell Kit, 48 rxns (PN-1000120), and Dual Index Kit TT Set A, 96 rxns (PN-1000215) were used. The concentration of each library was accurately determined through qPCR utilizing the KAPA library Quantification Kit according to the manufacturer's protocol (KAPA Biosystems/Roche) to produce cluster counts appropriate for the Illumina NovaSeq6000 instrument. Normalized libraries were sequenced on a NovaSeq6000 S4 Flow Cell using the XP workflow and a 50x10x16x150 sequencing recipe according to manufacturer protocol. A median sequencing depth of 50,000 reads/cell was targeted for each Gene Expression Library.

Aligning snRNA-seq reads

After sequencing, the Illumina output was processed using the CellRanger (v6.0.0) recommended pipeline to generate gene-barcode count matrices. A custom reference genome was made with the "cellranger mkref" command, using the fasta file of zebrafish reference genome GRCz11 constructed from the Ensemble genome build (https://useast.ensembl.org/Danio_rerio/Info/Index) and the sorted Gene Transfer Format file (v4.3.2) from the improved zebrafish transcriptome annotation (Lawson et al., 2020). Base call files for each sample from Illumina were demultiplexed into FASTQ reads. Then, the "cellranger count" pipeline was used to align sequencing reads in FASTQ files to the custom reference genome. Both exon and intron sequences were included during the alignment. The filtered gene-barcode count matrices generated by "cellranger count" was used for downstream analysis.

Integrated analysis of snRNA-seq dataset

All the datasets were integrated and analyzed using Seurat (v4.1.1) package with R (v4.2.1) (R Core Team, 2018; Stuart et al., 2019). Each sample count matrix was filtered for genes that were

expressed in at least 3 cells and cells expressing at least 200 genes, followed by cell quality assessment using commonly used QC matrixes (Ilicic et al., 2016). Cells having a unique number of genes between 200 to 4000 and a mitochondrial gene percentage <5 were used for downstream processing. Each dataset was independently normalized and scaled using the "SCTransform" function, which is an improved method for normalization, that performs a variance-stabilizing transformation using negative binomial regression (Hafemeister and Satija, 2019). Standard integration workflow of Seurat was used to identify shared sources of variation across experiments as well as mutual nearest neighbors (Butler et al., 2018; Haghverdi et al., 2018). Integration features were selected based on the top 4000 highly variable features using "SelectIntegrationFeatures" function (nfeatures = 4000), which was used as input for the "anchor.features" argument of the "FindIntegrationAnchors" function. PCA analysis was performed on the 4000 variable features and the top 50 principal components selected based on the elbow plot heuristic, which measures the contribution of variation in each component. These 50 principal components were used in "FindNeighbors" and "FindClusters" functions to perform graph-based clustering on a shared nearest neighbor graph (Levine et al., 2015; Xu and Su, 2015). Louvain algorithm was used for modularity optimization in clustering the cells using "FindClusters" function. The resolution parameter (res = 0.5) that determines the granularity of the clustering was selected by visually inspecting clusters with resolutions ranging 0.1 - 2.0 as well as clustree graphs (Zappia and Oshlack, 2018). Uniform Manifold Approximation and Reduction (UMAP) was used for non-linear dimensional reduction of the first 50 principal components and visualize the data using "RunUMAP" function (Becht et al., 2018). Data was graphed using different plot functions, such as "DimPlot", "VlnPlot", "FeaturePlot", "Dotplot" and "DoHeatmap", to view the cell cluster identity and marker gene expression. Cell proportion data was extracted using "table" and "prop.table" functions. Differential gene expression for individual cluster was identified using Wilcoxon rank sum test in the "FindAllMarkers" function. Marker genes detected in at least 25% of the clustered cells and with a logFC threshold of 0.25 were selected. Only positive markers were reported.

Subset analysis of neuron clusters

The neuron cell clusters identified from the complete dataset were subclustered using the "subset" function for subcluster analysis. The subset was again normalized and scaled using "SCTransform" function with glmGamPoi method (Ahlmann-Eltze and Huber, 2021). Fifty principal components were used, and the resolution parameter was set to 0.5. Further downstream analysis was done as described above for the integrated analysis. The top DE markers generated

for each neuron subcluster using “FindAllMarkers” function is given in the supplementary table S3.

Cluster identification using differentially expressed markers.

A “CNS markers” database of previously published markers of the different cell types that comprise the vertebrate brain and/or SC tissues was compiled (Guillemot, 2007; Zhang et al., 2014; Lu et al., 2015; Hernandez-Miranda et al., 2017; Tang et al., 2017; Haring et al., 2018; Hayashi et al., 2018; Rosenberg et al., 2018; Sathyamurthy et al., 2018; Zeisel et al., 2018; Baek et al., 2019; Rougeot et al., 2019; Tambalo et al., 2020; Cavone et al., 2021; Milich et al., 2021; Yadav et al., 2023). For each cell cluster, every marker gene identified as a top differentially expressed (DE) marker of that cluster was cross-referenced with our compiled “CNS markers” database. For every matching marker gene, one point was given to the respective cluster under the column name with the matching cell identity. Iteration over every marker gene was performed to generate a scoring matrix with varying points for each cluster against the different cell identities compiled in the “CNS markers” database (Table S2, scoring). Then, “phyper” function in R was used to calculate binomial probabilities using hypergeometric distribution for the total score obtained by each cluster against each cell identity in the database (Table S2, Binomial probability). Then, -log10 of probability values are obtained for plotting the heatmap (Table S2, -log10P). The resulting values were scaled to 0-100 and plotted as a heatmap using GraphPad prism. Each cluster was given an identity based on the maximum -log10 P score obtained in the heatmap. The top DE markers of clusters with ambiguous scores (e.g., 20, 24, 35 and 39) are manually searched in the literature for deciding cluster identity. “RenameIdents” function was used to assign identity to each cluster. For confirmation of the assigned cluster identity, enrichment of classical markers of respective cell types were tested using Dot plot. (https://github.com/vishnums007/Zebrafish-SCI-atlas/blob/main/s7_marker_comparison_v3.R)

Filtering differentially expressed markers for candidate gene selection.

To identify candidate genes that are uniquely expressed in N22 iNeurons, top DE markers were cross-checked and filtered against the top DE markers of all the other neuron subclusters. Enrichment and percent expression of these unique genes were then confirmed using Dot plots. Genes that were enriched or expressed in other neuronal or non-neuronal subclusters, in addition to their expression in iNeurons, were omitted. Genes that are exclusively enriched in iNeurons were selected for generating crispants.

Cell-cell interaction assay

The R package CellChat (v1.4.0) was used to evaluate regenerative cell-cell interactions after SCI (Jin et al., 2021). CellChat models the probability of cell-cell communication by integrating our gene expression data with a database (CellChatDB) of known interaction between signaling ligands, receptors, and their cofactors. CellChatDB is a manually curated from literature-supported ligand-receptor interactions in human and mouse, only. Therefore, we converted the normalized RNA data matrix of our zebrafish dataset at each timepoint into human orthologues using Ensemble biomaRT package (Durinck et al., 2009). The following rules were applied while converting the data matrix: 1) one-to-one orthologue mapping was performed whenever possible, 2) For genes with one to several human orthologues, the corresponding zebrafish RNA data value was copied to every mapped gene in humans, 3) RNA data values were eliminated for zebrafish genes that did not have any human orthologue, 4) RNA data values of paralogous zebrafish genes were added and the cumulative data value was assigned to the human orthologue (https://github.com/vishnums007/Zebrafish-SCI-atlas/blob/main/Sparse_matrix_homologe_converter_082322.R) . The converted RNA data was used then to create CellChat object using "createCellChat" function, followed by the recommended preprocessing functions with default parameters for the analysis of individual datasets. CellChatDB.human was used as the database for inferring cell-cell communication. All categories of ligand-receptor interactions in the database were used in the analysis. Communications involving less than 10 cells were excluded. Function "netAnalysis_computeCentrality" was used to calculate network centrality scores at each timepoint. Functions such as "netVisual_circle", "netAnalysis_contribution", "netVisual_aggregate", "netVisual_bubble" and "netAnalysis_signalingRole_heatmap" were used to generate different plots used in this paper.

Trajectory inference analysis

Pseudotime analysis was performed using CellRank (v1.5.1) package in Python (v3.8.10) (Rossum and Drake, 2009; Lange et al., 2022). Before analysis, the Seurat object was converted to an AnnData in a two-step process using the R package SeuratDisk (v0.9020). First, the Seurat object was saved as an h5Seurat file and then, converted it to an AnnData file to use as an input for pseudotime analysis using CellRank. Basic pre-processing of the AnnData file was performed with default recommended settings using the scvelo (v0.2.4) and scanpy (v1.9.1) packages. Genes expressed in at least 10 cells were included and 30 principal components and neighbors were used for preprocessing of the data. CytoTRACEkernel was used for pseudotime

computation and direct KNN graph-edges to point into the direction of increasing differentiation status (Gulati et al., 2020). The transition matrix was calculated by setting the threshold_scheme parameter to “soft” to reconstruct cellular trajectories using VIA algorithm (Stassen et al., 2021). This transition matrix was projected onto a UMAP plot to obtain a velocity graph.

Gene ontology

Gene ontology analysis was performed using Metascape (Zhou et al., 2019). Input and analysis species were set as D. rerio. Express analysis was performed for gene ontology. Metascape identified all statistically enriched terms (including GO biological processes, Reactome gene set and KEGG pathway), and calculated accumulative hypergeometric p-values and enrichment factors. Significant terms were hierarchically clustered into a tree based on Kappa-statistical similarities among their gene memberships. A kappa score of 0.3 was applied to cast the tree into term clusters. The most enriched term in each cluster was chosen as the representative term.

Cross-species comparison of DE markers

To compare the DE markers of iNeuron and RAG clusters, top markers identified using Wilcoxon rank sum test in the “FindAllMarkers” function were selected for iNeurons (clusters N18 and N22 in the zebrafish dataset) and for the RAG cluster (identified using markers used in *Matson et al., 2022* in the mouse dataset GSE172167). Marker genes detected in >25% of the clustered cells and with a logFC threshold of 0.25 were selected. Only positive markers were used. R package *ggvenn* (v0.1.9) was used to plot the venn diagram to compare the top markers of the 3 clusters. Metascape (Zhou et al., 2019) analysis using “multiple gene list” was used to generate the Gene Ontology comparison between zebrafish and mouse clusters.

Cross-species transcriptomics

Neuron subsets from zebrafish (Fig. 1) and mouse (GSE172167) datasets were used for cross-species data integration. Prior to integration, a custom made R script (as previously mentioned during CellChat analysis) was used to convert the RNA count matrix of zebrafish neurons into their mouse orthologues using the Ensemble biomaRT package (Durinck et al., 2009). The following rules were applied while converting the data matrix: 1) one-to-one orthologue mapping was performed when possible, 2) For genes with one to several mouse orthologues, the corresponding zebrafish RNA data value was copied to every mapped gene in mouse, 3) RNA data values were eliminated for zebrafish genes that did not have any mouse orthologue, 4) RNA data values of paralogous zebrafish genes were added and the cumulative data value was

assigned to the mouse orthologue. Following gene conversion, the zebrafish and mouse datasets were integrated using Seurat package with 6000 highly variable features. Resolution 1.1 was used for cluster analysis of the integrated dataset.

Histology

Sixteen µm cross cryosections of paraformaldehyde fixed SC tissues were used. Tissue sections were imaged using a Zeiss LSM 800 confocal microscope for immunofluorescence and hybridization chain reaction (HCR) RNA *in situ* hybridization.

The HCR RNA *in situ* hybridization protocol was adapted from Molecular Instruments (https://www.molecularinstruments.com/hcr-ihc-protocols) (Choi et al., 2018). Briefly, tissue sections were hydrated in PBS, dehydrated stepwise into 100% ethanol, then rehydrated stepwise into PBT (0.1% Tween-20 in PBS). Sections were pre-treated either with 0.2% TritonX-100 in PBS for 5 minutes or boiled in Citrate Buffer (10mM Citric Acid, 0.05% Tween-20, pH 6.0) for 10 minutes. For blocking, sections were incubated in Hybridization buffer (Molecular Instruments) for 1 hr at 37°C. For hybridization, sections were incubated in pre-warmed DNA probe sets diluted to 0.0015 pmol/uL in Hybridization buffer for 48 hrs at 37°C. Washes were then performed with Wash Buffer (Molecular Instruments) at 37°C followed by 5x SSCT (3M NaCl, 0.3 M Sodium Citrate, 0.1% Tween-20, pH 7.0). For signal amplification, sections were incubated in Amplification buffer (Molecular Instruments) for 1 hr at room temperature. Prior to amplification, h1 and h2 hairpins were snap-cooled in individual tubes by heating to 95°C and allowing tubes to return to ambient temperature slowly. For amplification, h1 and h2 snap-cooled hairpins were mixed together and diluted 1:50 in Amplification buffer. Amplification proceeded overnight at room temperature in the dark. Samples were then washed thoroughly in 5x SSCT, 5x SSC, and PBT at room temperature before proceeding to immunohistochemistry. HCR RNA probes used in this study (*syt11a, syt11b,* and *vamp4*) were designed using a python script. Probe sets were ordered as 50 pmol opools from IDT. Oligo sequences for each probe set are provided in Table S4.

For immunohistochemistry, tissue sections were hydrated in PBT then treated with blocking agent (5% goat serum in PBT) for 1 hr at room temperature. For nuclear antigens, sections were treated with 0.2% TritonX-100 in PBT for 5 minutes and washed thoroughly in PBT prior to the blocking step. Sections were incubated overnight at 4°C with respective primary antibodies diluted in blocking agent, then washed in PBT, and treated for 1 hour in secondary antibodies diluted in blocking agent at room temperature. For EdU staining, sections are incubated with freshly

prepared EdU staining solution (100mM Tris at pH 8.5 - SIGMA T6066, 1 mM $CuSO_4$ – SIGMA C1297, 200 µM Fluorescent azide – Thermo Fischer Scientific and 100 mM Ascorbic Acid - SIGMA A5960) for 30 minutes in the dark at room temperature (Salic and Mitchison, 2008). Following washes, sections were incubated in 1 µg/mL of Hoechst (Thermo Scientific, H3570) for 3 minutes, washed in PBT and mounted in Fluoromount-G mounting media (SouthernBiotech, 0100-01). Primary antibodies used in this study were chicken anti-GFP (AVES, 1020, 1:1000), rabbit anti-dsRed (Clontech, 632496, 1:250), mouse anti-HuC/D (Invitrogen, A21271, 1:500). Secondary antibodies (Invitrogen, 1:250) used in this study were Alexa Flour 488, Alexa Flour 594, and Alexa Flour 647 goat anti-rabbit or goat anti-mouse antibodies.

CRISPR/Cas9 mutagenesis

CRISPR/Cas9 design, mutagenesis and screening was performed as previously described (Klatt Shaw and Mokalled, 2021). Briefly, crRNA guide RNA sequences were selected using CHOPCHOP (https://chopchop.cbu.uib.no/). Only sequences with no off-target sites with three or fewer mismatches elsewhere in the genome were selected. To maximize the effect of small indels, target sites were chosen that lie within essential domains (Table S5). Alt-R tracrRNA and crRNA gRNAs (IDT, Cat# 1072534) were reconstituted using manufacturer's specifications as 100 µM stocks, then annealed at a final concentration of 50 µM. Alt-R S.p. Cas9 nuclease V3 (IDT, Cat# 1081059) was diluted in Cas9 dilution buffer (1 M HEPES at pH 7.5, 2 M KCl) to a working concentration of 25 µM. Annealed dgRNA duplexes were diluted 1:1 in duplex buffer (IDT, Cat# 11-05-01-03) to a working concentration of 25 µM. Equal volumes of dgRNA were added to Cas9 protein and incubated at 37°C for 5 minutes. For dual targeting of *syt11a* and *syt11b*, Cas9 protein was added in equal molar amounts to the total concentration of dgRNA. Tubingen wild-type embryos were injected with 1 nL of CRISPR/Cas9 solution at the one-cell stage and grown to adulthood for genotyping, SC surgeries and functional analysis. The full sequence for each guide RNAs is provided in Table S5.

Genotyping by capillary electrophoresis

Capillary electrophoresis was used to calculate the indel frequency for each CRISPR/Cas9 target site. For DNA extraction, whole 4 dpf larvae or ~3 mm of excised adult tail fins were added to 20 µL (larvae) or 50 µL (adult fin) of fin lysis buffer (10 mM Tris at pH 7.0, 50 mM KCl, 1 mM EDTA at pH 8.0, 0.3% Tween-20, freshly added Proteinase K at 200 µg/ml). DNA samples were incubated at 55°C for 60 minutes and then, followed by a 15-minute incubation at 95°C. 150-250 bp PCR products were generated using NEB Taq Polymerase (Cat# M0273) with gene-specific

primers (Table S5) in a volume of 10 μL in Pryme PCR semi-skirted PCR plates (MidSci, Cat# AVRT1). Samples were diluted to 24 μL in TE dilution buffer (Agilent, DNF-495-0060) and loaded into the 5200 Fragment Analyzer System (Agilent, Cat# M5310AA). Capillary electrophoresis was carried out using the Agilent Fragment Analyzer Qualitative DNA Kit (Cat# DNF-905-K1000) according to the manufacturer's specifications.

To calculate indel frequency, 2 wild-type control siblings were PCR amplified. The size of wild-type products was determined using these control samples. PCR products with peaks within 1 bp of control amplicon size were termed wild types (non-indel). Indel frequency was calculated by dividing the signal intensity of total non-indel peaks by the cumulative intensity of all peaks in each sample. Because of significant noise due to primers (<100 bp) and non-specific products (>300 bp) in wild-type samples, only signals between 100 and 300 bp were used to calculate indel frequency.

Swim endurance assay

Swim endurance assays were performed as previously described (Burris et al., 2021). Zebrafish were exercised in groups of 8-15 in a 5 L swim tunnel device (Loligo, Cat# SW100605L, 120V/60Hz). After 5 minutes of acclimation (with no flow) inside the enclosed tunnel, fish were swum at 9 cm/s and 10 cm/s for 5 minutes each to evaluate their swimming capability at bare minimum velocity. Water current velocity was then increased every two minutes and fish swam against the current until they reached exhaustion. Exhausted animals were removed from the chamber without disturbing the remaining fish. Swim time at exhaustion was recorded for each fish. Fish that were exhausted before the first 15 minutes were considered poorly recovered. Percent recovery was calculated by dividing the number of fish that swam more than 15 minutes to the total number of fish present in the group.

Swim behavior assay

Swim behavior assays were performed as previously described (Burris et al., 2021). Zebrafish were divided into groups of 5 in a 5 L swim tunnel device (Loligo, Cat# SW100605L, 120V/60Hz). Each group was allowed to swim for a total of 15 min under zero to low current velocities (5 min at 0 cm/s, 5 min at 10 cm/s, and 5 min at 15 cm/s). The entire swim session was recorded using high-speed camera (iDS, USB 3.0 color video camera) with following settings: aspect ratio, 1:4; pixel clock, 344; frame rate, 70 frames/s; exposure time: 0.29; aperture, 1.4 to 2; maximum frames; 63,000. Movies were converted to 20 frames/s and analyzed using a customized Fiji

macro (https://github.com/vishnums007/Zebrafish-SCI-atlas/blob/main/Swim%20behavior_Tracking_v2.ijm). For each frame, animals/objects >1500 px2 were identified, and the XY coordinates were derived for each animal/object. Each frame was independently analyzed, and animal/object tracking was completed using a customized R Studio script(https://github.com/vishnums007/Zebrafish-SCI-atlas/blob/main/SwimBehavior_processing%20and%20quantification_v7.R). The script aligned coordinates, calculated swim metrics considering three separate frame windows (Frames 0-6000 at 0 cm/s; frames 6001-12000 at 10 cm/s, and frames 12001-18001 at 20 cm/s). Distance swam was analyzed at 0, 10, and at 15 cm/s.

Axon tracing assay

Anterograde axon tracing was performed on adult zebrafish at 28 dpi as previously described (Mokalled et al., 2016). Fish were anaesthetized using MS-222 and fine scissors were used to transect the cord 4 mm rostral to the lesion site. Biocytin-soaked Gelfoam Gelatin Sponge was applied at the new injury site (Gelfoam, Pfizer, cat# 09-0315-08; Biocytin, saturated solution, Sigma, Cat# B4261). Fish were euthanized 3 hours post-treatment and Biocytin was histologically detected using Alexa Fluor 594-conjugated Streptavidin (Thermo Fisher, cat# S-11227). Biocytin-labeled axons were quantified using the “threshold” and “particle analysis” tools in the Fiji software. Four sections per fish at 0.5 (proximal) and 2 (distal) mm caudal to the lesion core, and 2 sections 1 mm rostral to the lesion, were analyzed. Axon growth was normalized to the efficiency of Biocytin labeling rostral to the lesion for each fish. The axon growth index was then normalized to the control group for each experiment.

Glial bridging assay

Gfap immunohistochemistry was performed on serial sections. The cross-sectional area of the glial bridge and the area of the intact SC rostral to the lesion were measured using ImageJ software. Bridging was calculated as a ratio of these measurements.

Quantification and statistical analysis

Cell counting. Cell counting were performed using a customized Fiji script (adapting ITCN plugin: Image based Tool for counting nuclei- https://imagej.nih.gov/ij/plugins/itcn.html, https://github.com/vishnums007/Zebrafish-SCI-atlas/blob/main/Cell_Counter_v1-5_vms.ijm). Orthogonal projections of individual image stacks were generated using Zen software. A customized Fiji script incorporated user-defined inputs to define channels (including Hoechst) and

to outline SC perimeters. To quantify nuclei, the following parameters were set in ITCN counter: width – 15; minimal distance – 7.5; threshold – 0.4. Once nuclei were identified, user-defined thresholds of individual cell markers were used to mask the image and identify nuclei located inside the masked regions. X/Y coordinates were extracted for each nucleus for cell counting. Raw counts and X/Y coordinates from Fiji were processed using a customized R script (https://github.com/vishnums007/Zebrafish-SCI-atlas/blob/main/Cell_Count_Processor_v1_vms.R). Markers that share nuclei with the same X/Y coordinates were considered overlapping.

Quantifying HCR in situ signal. HCR *in situ* hybridization signals were quantified using custom made Fiji script (https://github.com/vishnums007/Zebrafish-SCI-atlas/blob/main/hcr_celltypespecific_analysis_v3.1_080222.ijm). Orthogonal projections of individual image stacks were generated using the Zen software (Zeiss). ROIs around SC borders were defined to exclude non-SC tissues and user-defined thresholds were set to create an inverted mask. Background noise was either manually corrected or defined by thresholding a dedicated, unstained background channel. Integrated density was quantified for fluorescence signals inside the quantification mask using the "Analyze Particles" command. To calculate the HCR *in situ* hybridization signal inside neurons, an inverted mask was created after thresholding HuC/D^{+} neurons, then added to the final quantification mask. The fluorescence signals inside this newly generated mask were considered neuron specific.

Script availability

All the scripts used in the study is available in GitHub (https://github.com/vishnums007/Zebrafish-SCI-atlas).

Figure 1

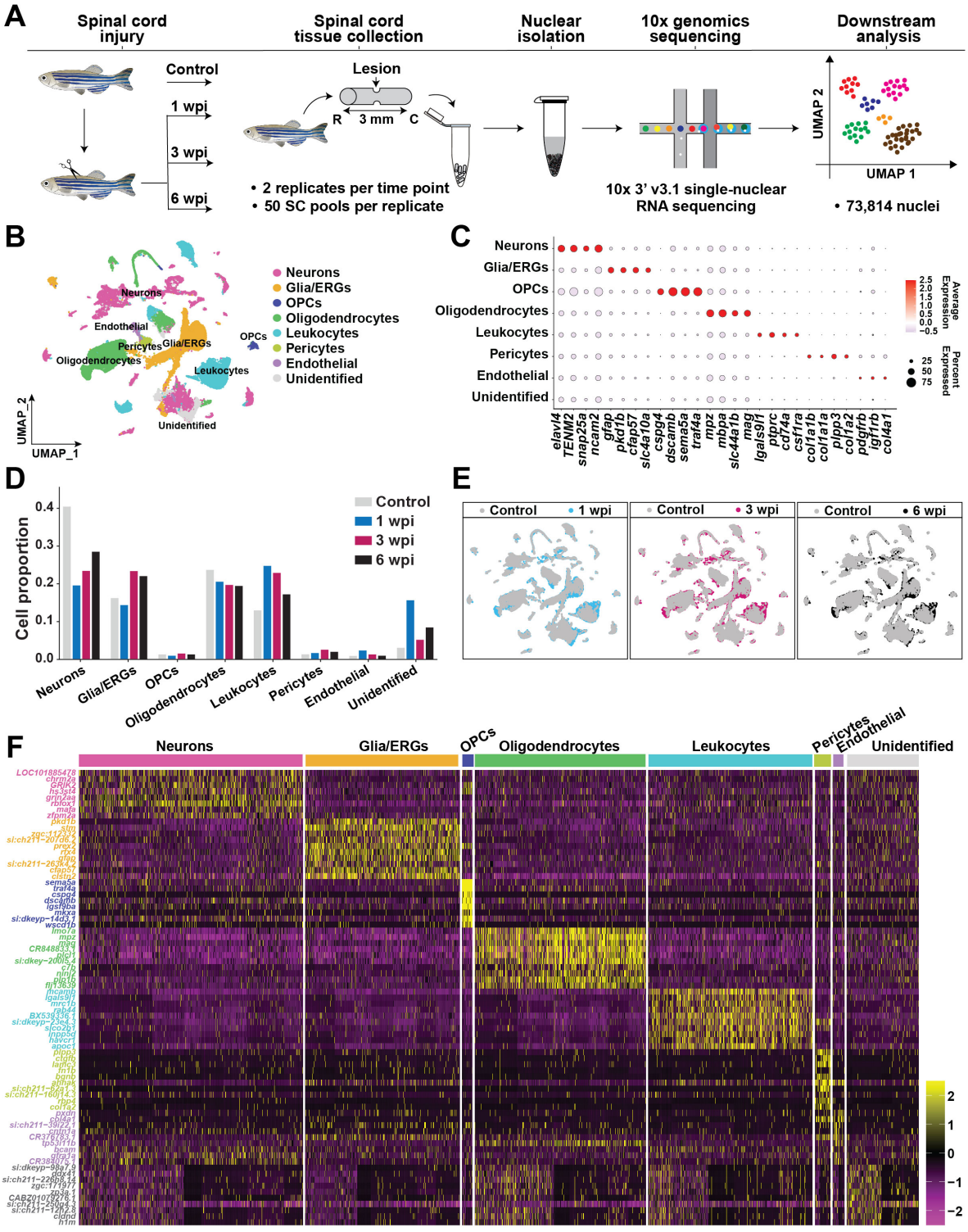
A
Spinal cord injury
Spinal cord tissue collection
Nuclear isolation
10x genomics sequencing
Downstream analysis
Control
1 wpi
3 wpi
6 wpi
Lesion
R
3 mm
C
• 2 replicates per time point
• 50 SC pools per replicate
10x 3' v3.1 single-nuclear RNA sequencing
UMAP 2
UMAP 1
• 73,814 nuclei
B
Neurons
Glia/ERGs
OPCs
Oligodendrocytes
Leukocytes
Pericytes
Endothelial
Unidentified
UMAP_2
UMAP_1
C
Average Expression
Percent Expressed
elavl4
TENM2
snap25a
ncam2
gfap
pkd1b
cfap57
slc4a10a
cspg4
dscamb
sema5a
traf4a
mpz
mbpa
slc44a1b
mag
lgals9l1
ptprc
cd74a
csf1ra
col1a1b
col1a1a
plpp3
col1a2
pdgfrb
igf1rb
col4a1
D
Cell proportion
Control
1 wpi
3 wpi
6 wpi
E
F

Figure 1. Transcriptomic profiling of innate SC repair in adult zebrafish. (A) Experimental pipeline to generate a single-cell atlas of zebrafish cells after SCI. SC tissue collection, nuclear isolation and single nuclear RNA-seq (snRNA-seq) were performed on wild-type fish were 1, 3 and 6 wpi. Uninjured SC nuclei were used as 0 wpi controls. 10x genomics sequencing with v3.1 chemistry was performed. Two biological replicates were used at each time point, and SC tissues from 50 animals were pooled into a single biological replicate. **(B)** Merged UMAP representation of the complete dataset. Two biological replicates, 4 time points and 73,814 cells were clustered into major spinal cell populations including neurons, glia/ependymo-radial glial cells (glia/ERGs), oligodendrocyte precursor cells (OPCs), and oligodendrocytes. **(C)** Marker gene expression in the major cell types identified after SCI. Dot plot shows canonical marker genes are enriched in their respective cell types identified. Dot colors and diameters represent average gene expression and percent cells with at least one UMI detected per gene, respectively. **(D)** Distribution of major cell types during SC regeneration. For each time point, cell proportions were to the total number of cells present at that time point. **(E)** Overlapping UMAP plots highlight broad changes in cell populations between 1, 3, or 6 wpi relative to uninjured controls. **(F)** Heatmap showing top 10 differentially expressed (DE) genes in the major cell populations identified by snRNA-seq. Yellow and magenta colors represent highly enriched and low-expression genes , repectively.

Figure 2

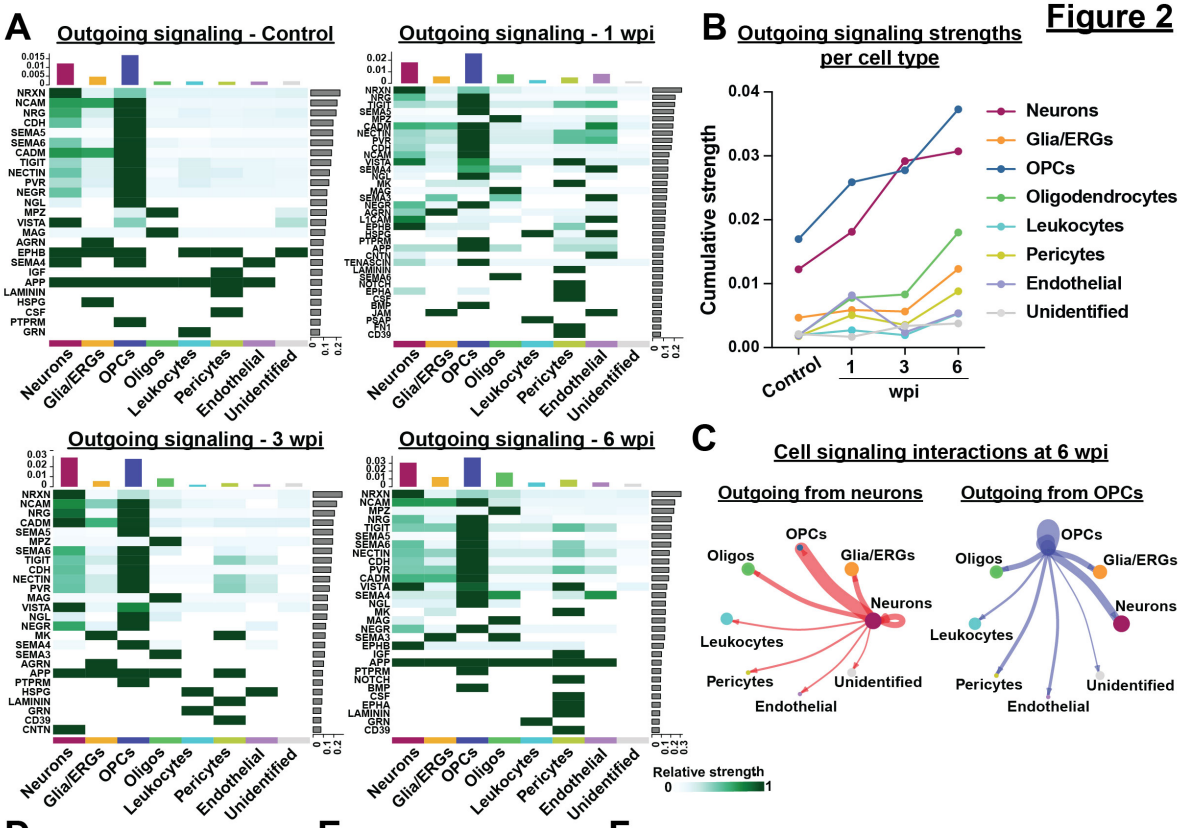

D Integrated outgoing signaling

Rank	Control	1 wpi	3 wpi	6 wpi
1	NRXN	NRXN	NRXN	NRXN
2	NCAM	NRG	NCAM	NCAM
3	NRG	TIGIT	NRG	MPZ
4	CDH	SEMA5	CADM	NRG
5	SEMA5	MPZ	SEMA5	TIGIT
6	SEMA6	CADM	MPZ	SEMA5
7	CADM	NECTIN	SEMA6	SEMA6
8	TIGIT	PVR	TIGIT	NECTIN
9	NECTIN	CDH	CDH	CDH
10	PVR	NCAM	NECTIN	PVR
11	NEGR	VISTA	PVR	CADM
12	NGL	SEMA4	MAG	VISTA
13	MPZ	NGL	VISTA	SEMA4
14	VISTA	MK	NGL	NGL
15	MAG	MAG	NEGR	MK
16	AGRN	SEMA3	MK	MAG
17	EPHB	NEGR	SEMA4	NEGR
18	SEMA4	AGRN	SEMA3	SEMA3
19	IGF	L1CAM	AGRN	EPHB
20	APP	EPHB	APP	IGF
21	LAMININ	HSPG	PTPRM	APP
22	HSPG	PTPRM	HSPG	PTPRM
23	CSF	APP	LAMININ	NOTCH
24	PTPRM	CNTN	GRN	BMP
25	GRN	TENASCIN	CD39	CSF
26		LAMININ	CNTN	EPHA
27		SEMA6		LAMININ
28		NOTCH		GRN
29		EPHA		CD39
30		CSF		
31		BMP		
32		JAM		
33		PSAP		
34		FN1		
35		CD39		

E Outgoing signaling from neurons

Rank	Control	1 wpi	3 wpi	6 wpi
1	NRXN	NRXN	NRXN	NRXN
2	NCAM	NRG	NCAM	NCAM
3	NRG	CADM	NRG	NRG
4	CDH	TIGIT	CADM	SEMA6
5	SEMA6	CDH	SEMA6	TIGIT
6	CADM	NECTIN	CDH	CDH
7	TIGIT	PVR	TIGIT	CADM
8	NECTIN	NCAM	NECTIN	MPZ
9	PVR	MPZ	PVR	NECTIN
10	VISTA	VISTA	VISTA	PVR
11	NEGR	SEMA5	MPZ	VISTA
12	NGL	EPHB	SEMA5	NEGR
13	SEMA5	NEGR	NEGR	EPHB
14	MAG	L1CAM	NGL	MAG
15	SEMA4	NGL	MAG	NGL
16	EPHB	AGRN	SEMA4	SEMA5
17	APP	SEMA4	APP	SEMA4
18		MAG	CNTN	APP
19		APP		
20		TENASCIN		
21		CNTN		
22		EPHA		

Enriched only at 1 wpi

Injury-induced genes

F

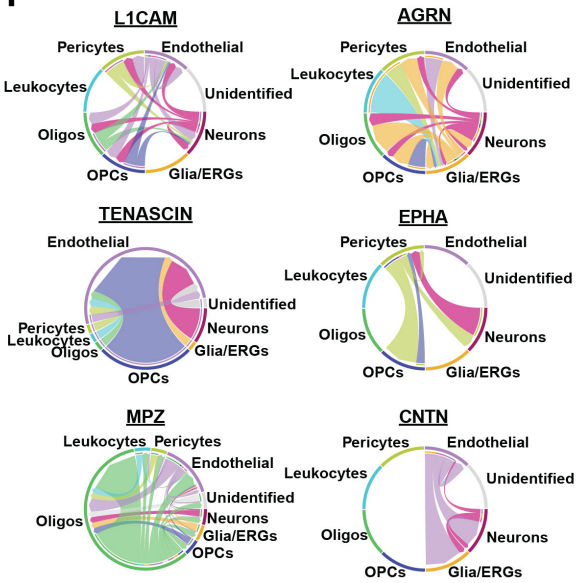

Figure 2. Cell-cell interaction networks during SC regeneration. (A,B) Relative strengths of outgoing signaling pathways in major spinal cell populations at 0, 1, 3 and 6 wpi. Bar graphs at the top of each heatmap show cumulative signaling strengths per cell population (A). Bar graphs at the right of each heatmap show cumulative signaling strength per pathway (A). Panel B shows elevated and dynamic cumulative strengths of signaling pathways outgoing from neurons and OPCs. **(C)** Circle plots represent cell-cell interaction strengths of signaling pathways outgoing from neurons and OPCs at 6 wpi. Arrow thickness is directly proportional to the cumulative strengths of all predicted interactions between clusters. **(D,E)** Outgoing signaling pathways for the complete dataset in D and for the neuron clusters in E. Pathways are ranked in the descending order of their cumulative signal strengths. Pathways highlighted in magenta represent injury-enriched signaling. Pathways highlighted in magenta and yellow represent signaling pathways that are specifically enriched at 1 wpi. **(F)** Chord diagrams showing intercellular communication of signaling pathways that are enriched in neurons after SCI. Arc diameters are proportional to cumulative signaling strengths.

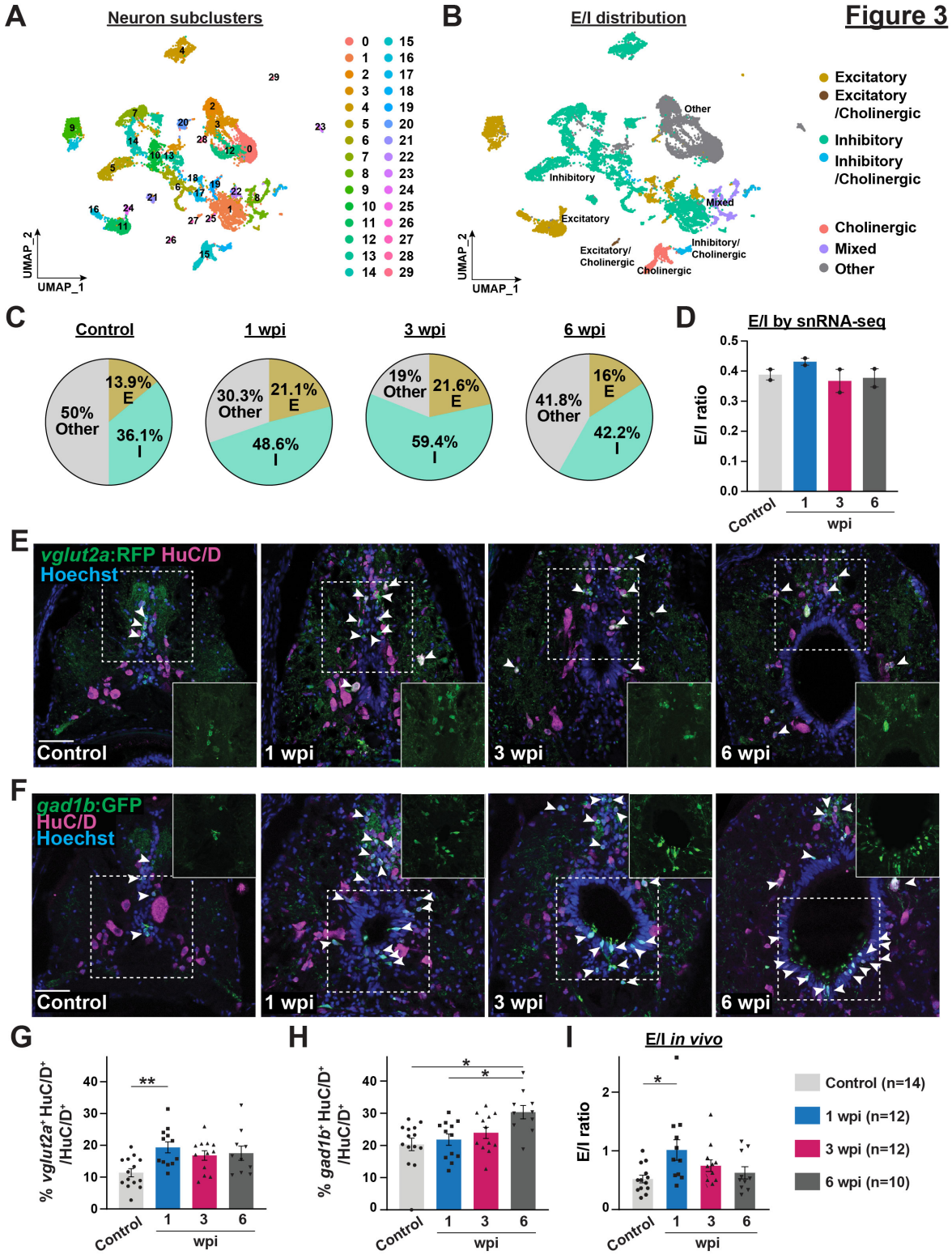
Figure 3
A
Neuron subclusters
UMAP_2
UMAP_1
B
E/I distribution
Excitatory
Excitatory /Cholinergic
Inhibitory
Inhibitory /Cholinergic
Cholinergic
Mixed
Other
Inhibitory
Excitatory
Excitatory/ Cholinergic
Cholinergic
Inhibitory/ Cholinergic
C
Control
1 wpi
3 wpi
6 wpi
50% Other
13.9% E
36.1% I
30.3% Other
21.1% E
48.6% I
19% Other
21.6% E
59.4% I
41.8% Other
16% E
42.2% I
D
E/I by snRNA-seq
E/I ratio
wpi
E
vglut2a:RFP HuC/D
Hoechst
Control
1 wpi
3 wpi
6 wpi
F
gad1b:GFP
HuC/D
Hoechst
Control
1 wpi
3 wpi
6 wpi
G
% vglut2a+ HuC/D+ /HuC/D+
H
% gad1b+ HuC/D+ /HuC/D+
I
E/I in vivo
E/I ratio
Control (n=14)
1 wpi (n=12)
3 wpi (n=12)
6 wpi (n=10)

Figure 3. Recovery of excitatory/inhibitory balance during SC regeneration. (A) UMAP plot showing 30 different neuron subclusters identified with 0.5 resolution parameter. **(B)** Classification of neuron clusters based on neurotransmitter properties. Canonical neurotransmitter marker genes are used: *slc17a6a* and *slc17a6b* for excitatory neurons; *slc6a5, gad1a, gad1b* and *gad2* for inhibitory neurons, *chata* and *slc5a7a* for cholinergic neurons. Excitatory/cholinergic and inhibitory/cholinergic neurons express cholinergic marker genes along with either excitatory or inhibitory markers, respectively. An ambiguous "Mixed" neuron cluster that expresses excitatory and inhibitory neurotransmitter genes. Neuron subclusters that do not express any of the previously mentioned marker genes are labelled "Other". **(C)** Pie charts show the proportions of excitatory, inhibitory, and "other" neuron populations at 0, 1, 3 and 6 wpi. In this analysis, excitatory neurons comprise excitatory and excitatory/cholinergic neurons. Inhibitory neurons comprise inhibitory and inhibitory/cholinergic neurons. The "Mixed" neuron population was not included in the quantification. **(D)** *in silico* calculation of E/I ratios during SC regeneration. Bar charts depict the ratio between excitatory and inhibitory neurons at 0, 1, 3 and 6 wpi. Dots indicate single biological replicates. Two biological replicates are shown per time point. Error bars represent SEM. **(E,F)** Immunostaining for RFP, GFP, HuC/D and Hoechst in SC cross sections from Tg(*vglut2a*:RFP) and Tg(*gad1b*:GFP) zebrafish at 0, 1, 3 and 6 wpi. White arrows point to RFP^+ HuC/D^+ neurons in E and GFP^+ HuC/D^+ neurons in F. Insets depict single channel views of *vglut2a*:RFP or *gad1b*:GFP in dorsal and ventral SC domains, respectively. **(G,H)** Quantification of glutamatergic and GABAergic neurons after SCI. Percent *vglut2a*$^+$ HuC/D^+ neurons (ANOVA p-value: 0.0086) and *gad1b*$^+$ HuC/D^+ neurons (ANOVA p-value: 0.0043) were normalized to the total number of HuC/D^+ neurons. **(K)** *in vivo* quantification of E/I ratios during SC regeneration. Ratios of glutamatergic to GABAergic neurons were calculated at 0, 1, 3 and 6 wpi (ANOVA p-value: 0.03421). Solid circles and polygons in bar charts indicate individual animals and sample sizes are indicated in parentheses. SC cross sections 450 μm rostral to the lesion were analyzed. Brown-Forsythe and Welch ANOVA test was performed in G, H and I with Dunnett's T3 multiple comparisons test performed across different timepoints having 95% CI. * $p \leq 0.05$, ** $p \leq 0.01$; Scale bars, 50 μm.

Figure 4

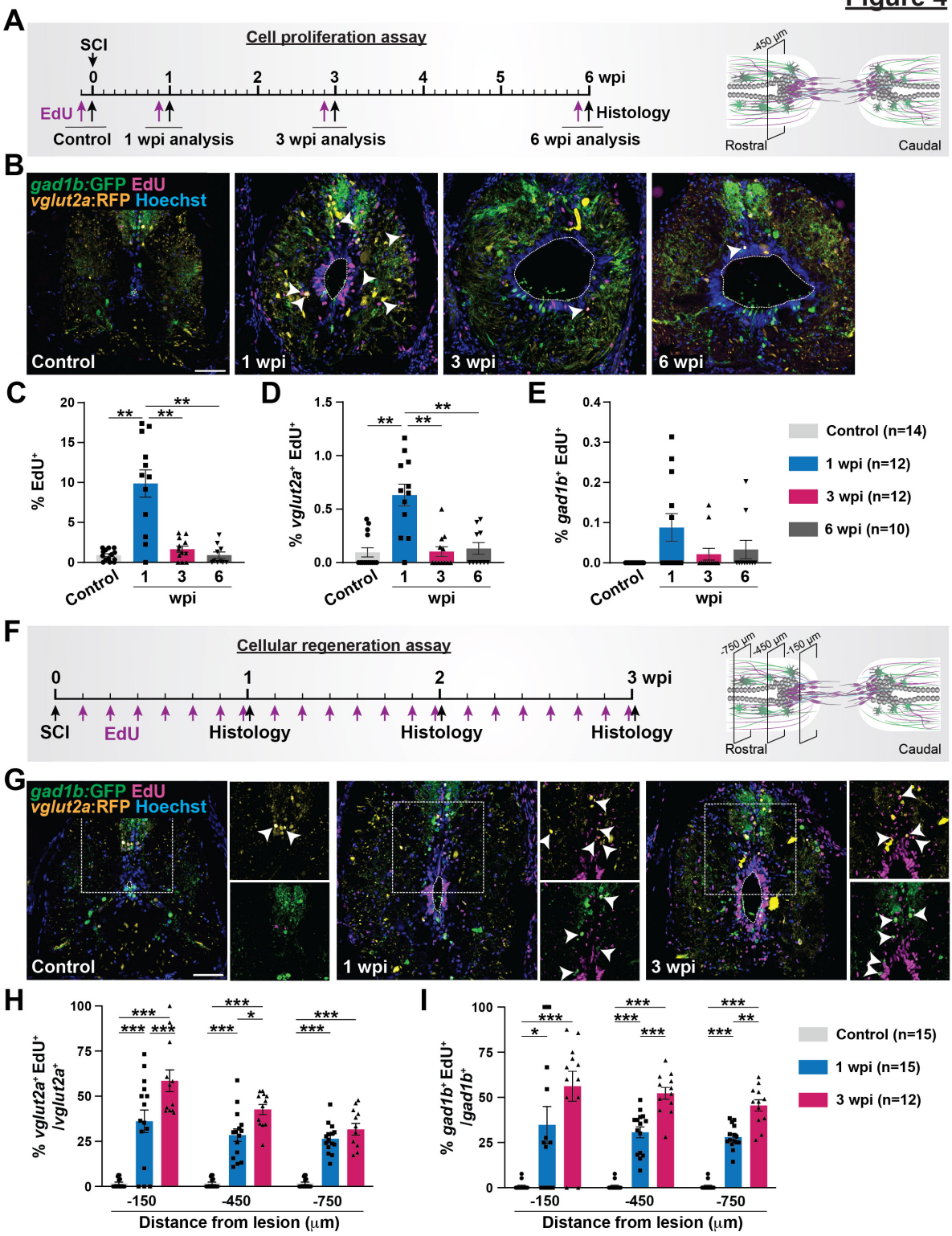
A
Cell proliferation assay
SCI
0
1
2
3
4
5
6 wpi
EdU
Histology
Control
1 wpi analysis
3 wpi analysis
6 wpi analysis
-450 µm
Rostral
Caudal
B
gad1b:GFP EdU
vglut2a:RFP Hoechst
Control
1 wpi
3 wpi
6 wpi
C
% EdU+
Control
1
3
6
wpi
D
% vglut2a+ EdU+
E
% gad1b+ EdU+
Control (n=14)
1 wpi (n=12)
3 wpi (n=12)
6 wpi (n=10)
F
Cellular regeneration assay
0
1
2
3 wpi
SCI
EdU
Histology
-750 µm
-450 µm
-150 µm
G
H
% vglut2a+ EdU+ /vglut2a+
-150
-450
-750
Distance from lesion (µm)
I
% gad1b+ EdU+ /gad1b+
Control (n=15)
1 wpi (n=15)
3 wpi (n=12)

Figure 4. Regeneration of excitatory and inhibitory neurons after SCI. (A) Experimental timeline to assess cell proliferation at 1, 3 and 6 wpi. Tg(*vglut2a*:RFP; *gad1b*:GFP) zebrafish were subjected to SC transections. Single intraperitoneal EdU injections were performed at either 6, 20, or 41 days post-injury. SC tissues were harvested for analysis at 1, 3, or 6 wpi and at 24 hours after EdU injection. Uninjured animals were injected with EdU and collected 24 hours after EdU injection as controls. SC cross-section 450 µm rostral to the lesion was used for quantifications. **(B)** Staining for RFP, GFP, EdU and Hoechst in SC cross sections of Tg(*vglut2a*:RFP; *gad1b*:GFP) zebrafish at 0, 1, 3 and 6 wpi. White arrows indicate *vglut2a*$^+$ EdU$^+$ neurons. Dotted lines delineate central canal edges. **(C-E)** Quantification of EdU$^+$ cells (ANOVA p-value <0.0001), *vglut2a*$^+$ EdU$^+$ neurons (ANOVA p-value <0.0001) and *gad1b*$^+$ EdU$^+$ neurons (ANOVA p-value: 0.0449) at 0, 1, 3 and 6 wpi. Percent cells were normalized to the total number of nuclei in SC sections. **(F)** Experimental timeline to assess the cumulative profiles of regenerating neurons at 1 and 3 wpi. Tg(*vglut2a*:RFP; *gad1b*:GFP) zebrafish were subjected to SC transections and daily intraperitoneal EdU injections. SC tissues were harvested for analysis at 1, 2 or 3 wpi. Control SCs received daily EdU injection for 7 days before collection. Tissue sections 150, 450 and 750 µm rostral to the lesion were analyzed. **(G)** Staining for RFP, GFP, EdU and Hoechst in SC cross sections of Tg(*vglut2a*:RFP; *gad1b*:GFP) zebrafish at 0, 1 and 3 wpi. White arrows indicate *vglut2a*$^+$ EdU$^+$ neurons. Insets show single channel views of *vglut2a*:RFP and *gad1b*:GFP expression. Dotted lines delineate central canal edges. **(H,I)** Quantification of regenerating glutamatergic neurons (*vglut2a*$^+$ EdU$^+$) (ANOVA p-value <0.0001) and regenerating GABAergic neurons (*gad1b*$^+$ EdU$^+$) (ANOVA p-value <0.0001). For each section, percent cells were normalized to the number of *vglut2a*$^+$ EdU$^+$ neurons in H and *vglut2a*$^+$ EdU$^+$ neurons in I. Brown-Forsythe and Welch ANOVA test was performed in C, D and E with Dunnett's T3 multiple comparisons test performed across different time points with 95% CI. Two-way ANOVA was performed in H and I with Tukey's multiple comparison test having 95% CI. * p≤0.05, ** p ≤0.01, *** p≤0.001. Solid circles and polygons in the bar charts indicate individual animals and sample sizes are indicated in parentheses. Scale bars, 50 µm.

Figure 5

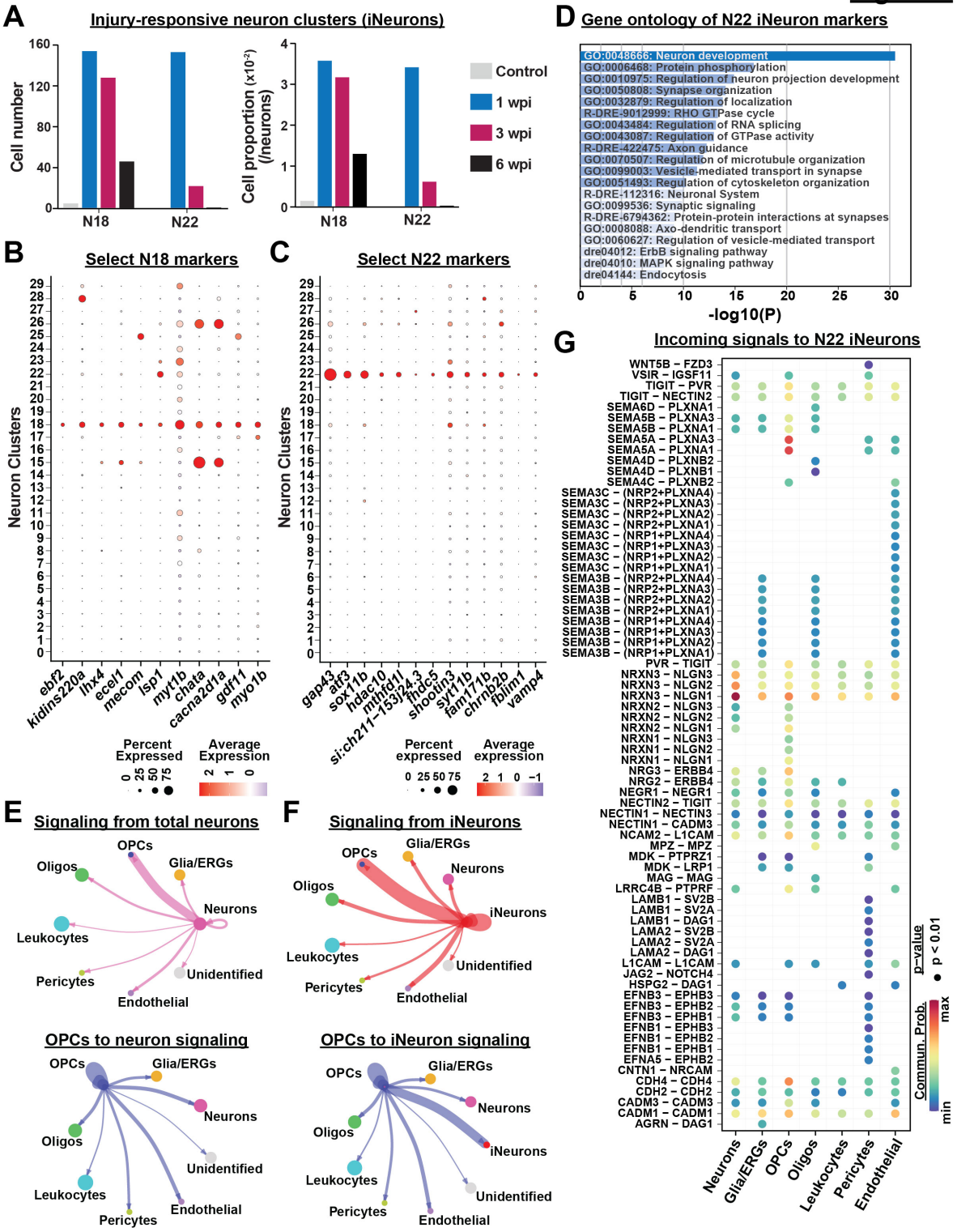
A
Injury-responsive neuron clusters (iNeurons)
Cell number
Cell proportion (x10⁻²) (/neurons)
N18
N22
Control
1 wpi
3 wpi
6 wpi
B
Select N18 markers
C
Select N22 markers
Neuron Clusters
ebf2
kidins220a
lhx4
ecel1
mecom
lsp1
myt1b
chata
cacna2d1a
gdf11
myo1b
gap43
atf3
sox11b
hdac10
mthfd1l
si:ch211-153j24.3
fhdc5
shootin3
syt11b
fam171b
chrnb2b
fblim1
vamp4
Percent Expressed
Average Expression
Percent expressed
Average expression
D
Gene ontology of N22 iNeuron markers
GO:0048666: Neuron development
GO:0006468: Protein phosphorylation
GO:0010975: Regulation of neuron projection development
GO:0050808: Synapse organization
GO:0032879: Regulation of localization
R-DRE-9012999: RHO GTPase cycle
GO:0043484: Regulation of RNA splicing
GO:0043087: Regulation of GTPase activity
R-DRE-422475: Axon guidance
GO:0070507: Regulation of microtubule organization
GO:0099003: Vesicle-mediated transport in synapse
GO:0051493: Regulation of cytoskeleton organization
R-DRE-112316: Neuronal System
GO:0099536: Synaptic signaling
R-DRE-6794362: Protein-protein interactions at synapses
GO:0008088: Axo-dendritic transport
GO:0060627: Regulation of vesicle-mediated transport
dre04012: ErbB signaling pathway
dre04010: MAPK signaling pathway
dre04144: Endocytosis
-log10(P)
E
Signaling from total neurons
OPCs
Glia/ERGs
Oligos
Neurons
Leukocytes
Pericytes
Unidentified
Endothelial
OPCs to neuron signaling
F
Signaling from iNeurons
iNeurons
OPCs to iNeuron signaling
G
Incoming signals to N22 iNeurons
WNT5B – FZD3
VSIR – IGSF11
TIGIT – PVR
TIGIT – NECTIN2
SEMA6D – PLXNA1
SEMA5B – PLXNA3
SEMA5B – PLXNA1
SEMA5A – PLXNA3
SEMA5A – PLXNA1
SEMA4D – PLXNB2
SEMA4D – PLXNB1
SEMA4C – PLXNB2
SEMA3C – (NRP2+PLXNA4)
SEMA3C – (NRP2+PLXNA3)
SEMA3C – (NRP2+PLXNA2)
SEMA3C – (NRP2+PLXNA1)
SEMA3C – (NRP1+PLXNA4)
SEMA3C – (NRP1+PLXNA3)
SEMA3C – (NRP1+PLXNA2)
SEMA3C – (NRP1+PLXNA1)
SEMA3B – (NRP2+PLXNA4)
SEMA3B – (NRP2+PLXNA3)
SEMA3B – (NRP2+PLXNA2)
SEMA3B – (NRP2+PLXNA1)
SEMA3B – (NRP1+PLXNA4)
SEMA3B – (NRP1+PLXNA3)
SEMA3B – (NRP1+PLXNA2)
SEMA3B – (NRP1+PLXNA1)
PVR – TIGIT
NRXN3 – NLGN3
NRXN3 – NLGN2
NRXN3 – NLGN1
NRXN2 – NLGN3
NRXN2 – NLGN2
NRXN2 – NLGN1
NRXN1 – NLGN3
NRXN1 – NLGN2
NRXN1 – NLGN1
NRG3 – ERBB4
NRG2 – ERBB4
NEGR1 – NEGR1
NECTIN2 – TIGIT
NECTIN1 – NECTIN3
NECTIN1 – CADM3
NCAM2 – L1CAM
MPZ – MPZ
MDK – PTPRZ1
MDK – LRP1
MAG – MAG
LRRC4B – PTPRF
LAMB1 – SV2B
LAMB1 – SV2A
LAMB1 – DAG1
LAMA2 – SV2B
LAMA2 – SV2A
LAMA2 – DAG1
L1CAM – L1CAM
JAG2 – NOTCH4
HSPG2 – DAG1
EFNB3 – EPHB3
EFNB3 – EPHB2
EFNB3 – EPHB1
EFNB1 – EPHB3
EFNB1 – EPHB2
EFNB1 – EPHB1
EFNA5 – EPHB2
CNTN1 – NRCAM
CDH4 – CDH4
CDH2 – CDH2
CADM3 – CADM3
CADM1 – CADM1
AGRN – DAG1
p-value
p < 0.01
Commun. Prob.
max
min

Figure 5. Emergence of an injury-responsive iNeuron signature during SC regeneration. (A) Numbers and proportions of N18 and N22 iNeurons at 0, 1, 3 and 6 wpi. **(B,C)** Marker gene expression for N18 (B) and N22 iNeurons (C). Dot plot shows select DE marker genes. Dot colors and diameters represent average gene expression and percent cells with at least one UMI detected per gene, respectively. **(D)** Gene ontology of N22 iNeuron DE markers. Twenty of the most enriched terms are shown. X-axis represents -log10(p-value) for each term. **(E,F)** Circle plots represent cell-cell interaction strengths at 6 wpi. Signaling pathways outgoing from total neurons and from OPCs to total neurons are shown in E. Signaling pathways outgoing from iNeurons and from OPCs to iNeurons are shown in F. Arrow thickness is directly proportional to the cumulative strengths of all predicted interactions between clusters. **(G)** Bubble plot shows significant ligand-receptor interaction pair of signaling pathways incoming to iNeurons at 1 wpi. Dot colors and diameters represent interaction probabilities and p-values, respectively.

Figure 6

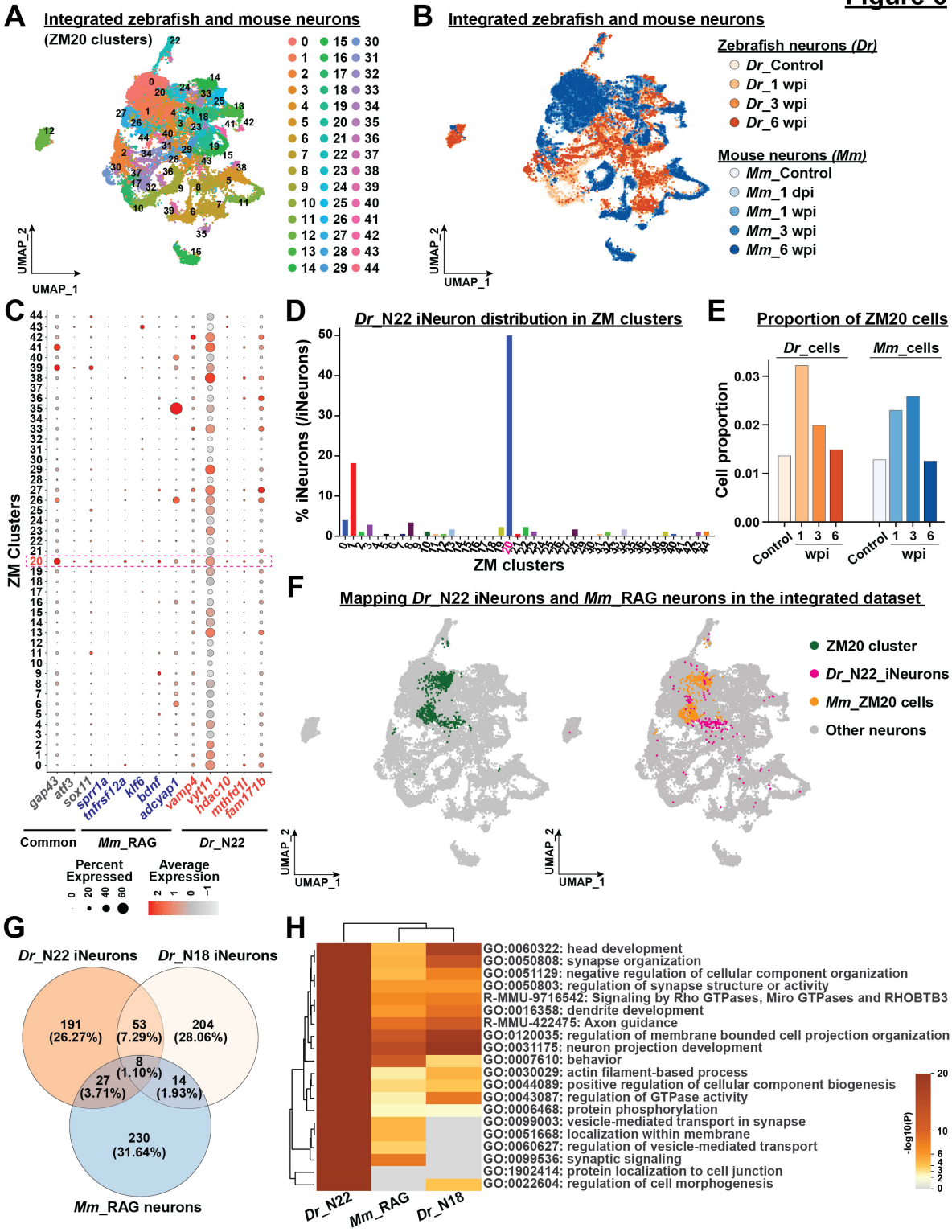
A
Integrated zebrafish and mouse neurons
(ZM20 clusters)
UMAP_1
UMAP_2
B
Integrated zebrafish and mouse neurons
Zebrafish neurons (Dr)
Dr_Control
Dr_1 wpi
Dr_3 wpi
Dr_6 wpi
Mouse neurons (Mm)
Mm_Control
Mm_1 dpi
Mm_1 wpi
Mm_3 wpi
Mm_6 wpi
C
ZM Clusters
gap43
atf3
sox11
sprr1a
tnfrsf12a
klf6
bdnf
adcyap1
vamp4
vyt11
hdac10
mthfd1l
fam171b
Common
Mm_RAG
Dr_N22
Percent Expressed
Average Expression
D
Dr_N22 iNeuron distribution in ZM clusters
% iNeurons (/iNeurons)
ZM clusters
E
Proportion of ZM20 cells
Dr_cells
Mm_cells
Cell proportion
Control
wpi
F
Mapping Dr_N22 iNeurons and Mm_RAG neurons in the integrated dataset
ZM20 cluster
Dr_N22_iNeurons
Mm_ZM20 cells
Other neurons
G
Dr_N22 iNeurons
Dr_N18 iNeurons
191 (26.27%)
53 (7.29%)
204 (28.06%)
8 (1.10%)
27 (3.71%)
14 (1.93%)
230 (31.64%)
Mm_RAG neurons
H
GO:0060322: head development
GO:0050808: synapse organization
GO:0051129: negative regulation of cellular component organization
GO:0050803: regulation of synapse structure or activity
R-MMU-9716542: Signaling by Rho GTPases, Miro GTPases and RHOBTB3
GO:0016358: dendrite development
R-MMU-422475: Axon guidance
GO:0120035: regulation of membrane bounded cell projection organization
GO:0031175: neuron projection development
GO:0007610: behavior
GO:0030029: actin filament-based process
GO:0044089: positive regulation of cellular component biogenesis
GO:0043087: regulation of GTPase activity
GO:0006468: protein phosphorylation
GO:0099003: vesicle-mediated transport in synapse
GO:0051668: localization within membrane
GO:0060627: regulation of vesicle-mediated transport
GO:0099536: synaptic signaling
GO:1902414: protein localization to cell junction
GO:0022604: regulation of cell morphogenesis
-log10(P)
Dr_N22
Mm_RAG
Dr_N18

Figure 6. Cross-species transcriptional comparisons between zebrafish and mouse neurons. (A,B) UMAP plot showing 45 distinct clusters in the integrated ZM dataset of mouse (*Mm*) and zebrafish (*Dr*) neurons at 1.1 resolution parameter. Dot colors represent cluster identity in A and the species of origin of each cell in B. **(C)** Dot plot represent the expression of N22 iNeuron and mouse RAG marker genes in the integrated ZM datset. Dot colors and diameters represent average gene expression and percent cells with at least one UMI detected per gene, respectively. Cluster ZM20 of the integrated ZM dataset shows enriched expression of 12/13 genes, and is highlighted in the dotted rectangular box. **(D)** Distribution of N22 iNeurons in the integrated ZM dataset. Cluster ZM 20 shows the highest proportion of N22 iNeurons and is highlighted in magenta. **(E)** Proportion of cluster ZM20 cells in the zebrafish and mouse datasets at different time points after SCI. **(F)** UMAP plots highlight zebrafish N22 iNeurons and mouse RAG neurons in the integrated ZM dataset. **(G)** Venn diagram ccomparing the top DE markers of zebrafish N22 iNeurons, zebrafish N18 iNeurons and mouse RAG neurons. The numbers and proportions of genes are shown for each section. **(H)** Gene ontology for the top DE markers of zebrafish N22 iNeurons, and zebrafish N18 iNeurons and mouse RAG neurons. Color gradients indicate -log10(p-value). Dendrograms on the left and top of the heatmap represent hierarchical clustering of GO terms.

Figure 7

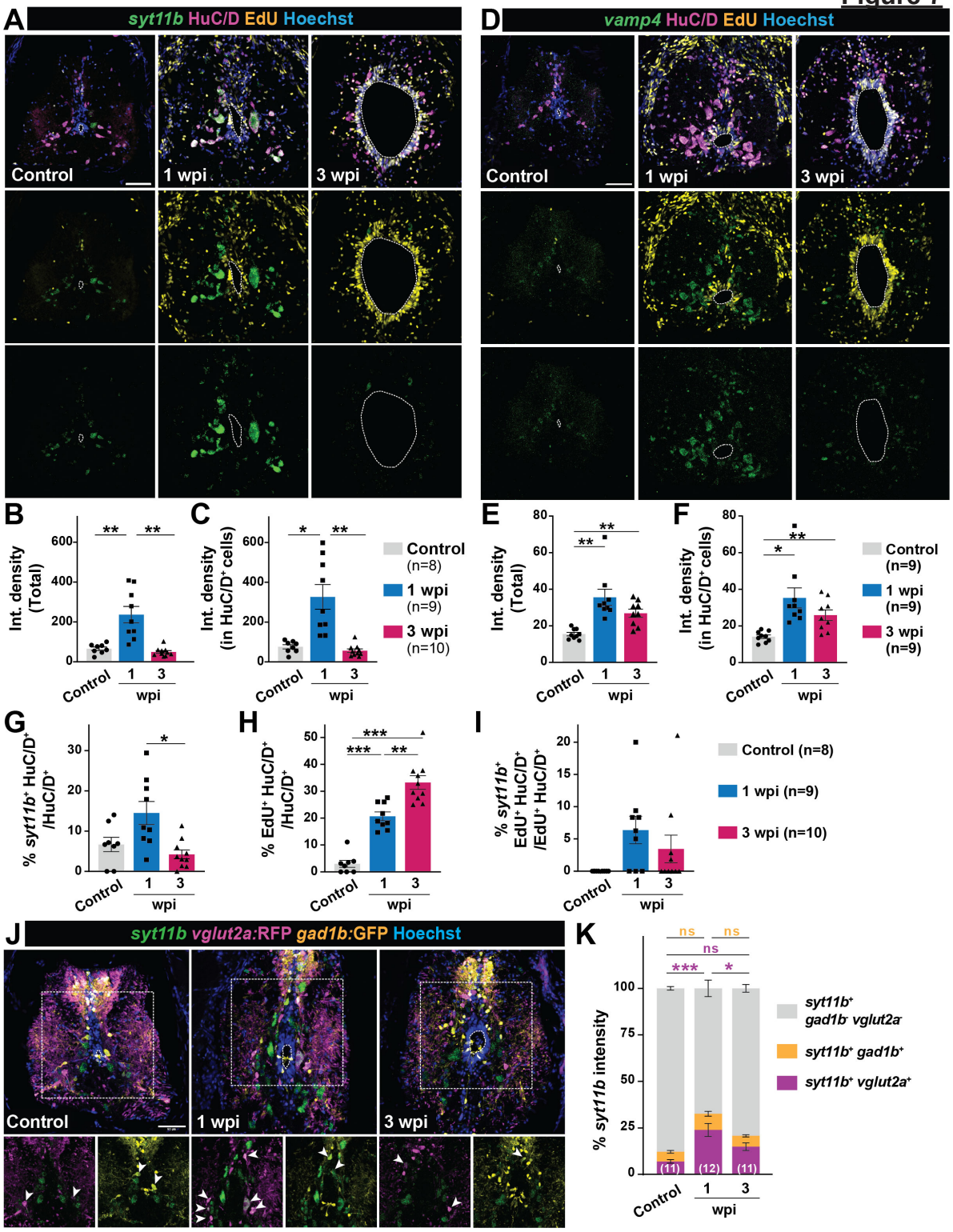
A
syt11b HuC/D EdU Hoechst
Control
1 wpi
3 wpi
D
vamp4 HuC/D EdU Hoechst
Control
1 wpi
3 wpi
B
Int. density (Total)
Control
1
3
wpi
C
Int. density (in HuC/D+ cells)
Control (n=8)
1 wpi (n=9)
3 wpi (n=10)
E
Int. density (Total)
F
Int. density (in HuC/D+ cells)
Control (n=9)
1 wpi (n=9)
3 wpi (n=9)
G
% syt11b+ HuC/D+ /HuC/D+
H
% EdU+ HuC/D+ /HuC/D+
I
% syt11b+ EdU+ HuC/D+ /EdU+ HuC/D+
Control (n=8)
1 wpi (n=9)
3 wpi (n=10)
J
syt11b vglut2a:RFP gad1b:GFP Hoechst
Control
1 wpi
3 wpi
K
% syt11b intensity
ns
***
*
(11)
(12)
(11)
syt11b+ gad1b- vglut2a-
syt11b+ gad1b+
syt11b+ vglut2a+

Figure 7. *in vivo* mapping of N22 iNeurons in zebrafish spinal tissues. (A) HCR *in situ* hybridization for *syt11b* and staining for HuC/D, Hoechst and EdU were performed on wild-type SC cross sections at 0, 1 and 3 wpi. Dotted lines delineate central canal edges. **(B,C)** Quantification of *syt11b* HCR *in situ* hybridization. Integrated density was calculated in the whole SC cross sections (ANOVA p-value: 0.0007) and inside HuC/D$^+$ neurons (ANOVA p-value: 0.0009) at 0, 1 and 3 wpi. **(D)** HCR *in situ* hybridization for *vamp4* and staining for HuC/D, Hoechst and EdU were performed on wild-type SC cross sections at 0, 1 and 3 wpi. Dotted lines delineate central canal edges. **(E,F)** Quantification of *vamp4* HCR *in situ* hybridization. Integrated density was calculated in the whole SC cross sections (ANOVA p-value: 0.0012) and inside HuC/D$^+$ neurons (ANOVA p-value: 0.0043) at 0, 1 and 3 wpi. **(G-I)** Quantification of *syt11b* expressing cells after SCI. Percent *syt11b*$^+$ HuC/D$^+$ neurons (normalized to HuC/D$^+$ neurons in G) (ANOVA p-value: 0.0062), percent EdU$^+$ HuC/D$^+$ neurons (normalized to HuC/D$^+$ neurons in H) (ANOVA p-value <0.0001), and percent *syt11b*$^+$ EdU$^+$ HuC/D$^+$ neurons (normalized to EdU$^+$ HuC/D$^+$ neurons in I) (ANOVA p-value: 0.0813). Analysis was performed on whole SC cross sections at 0, 1 and 3 wpi. **(J)** HCR *in situ* hybridization for *syt11b* in SC cross-sections of Tg(*vglut2a*:RFP; *gad1b*:GFP) zebrafish at 0, 1 and 3 wpi. Dotted lines delineate central canal edges. White arrowheads point to overlapping of *syt11b* transcripts with either *vglut2a* or *gad1b*. **(K)** Quantification of *syt11b* transcripts within *vglut2a*$^+$ and *gad1b*$^+$ neurons at 0, 1 and 3 wpi (ANOVA p-value <0.0001). *syt11b* signal outside either of these neurotransmitter populations was also quantified. SC cross sections at 450 µm rostral to the lesion were analyzed. Solid circles and polygons in the bar charts indicate individual animals and sample sizes are indicated in parentheses. Brown-Forsythe and Welch ANOVA test was performed in B, C, E, F, G, H, and I with Dunnett's T3 multiple comparisons test performed across different timepoints with 95% CI. Two-way ANOVA was performed in K with Tukey's multiple comparisons test with 95 % CI. * p≤0.05, ** p ≤0.01, *** p≤0.001. Scale bars, 50 µm

Figure 8

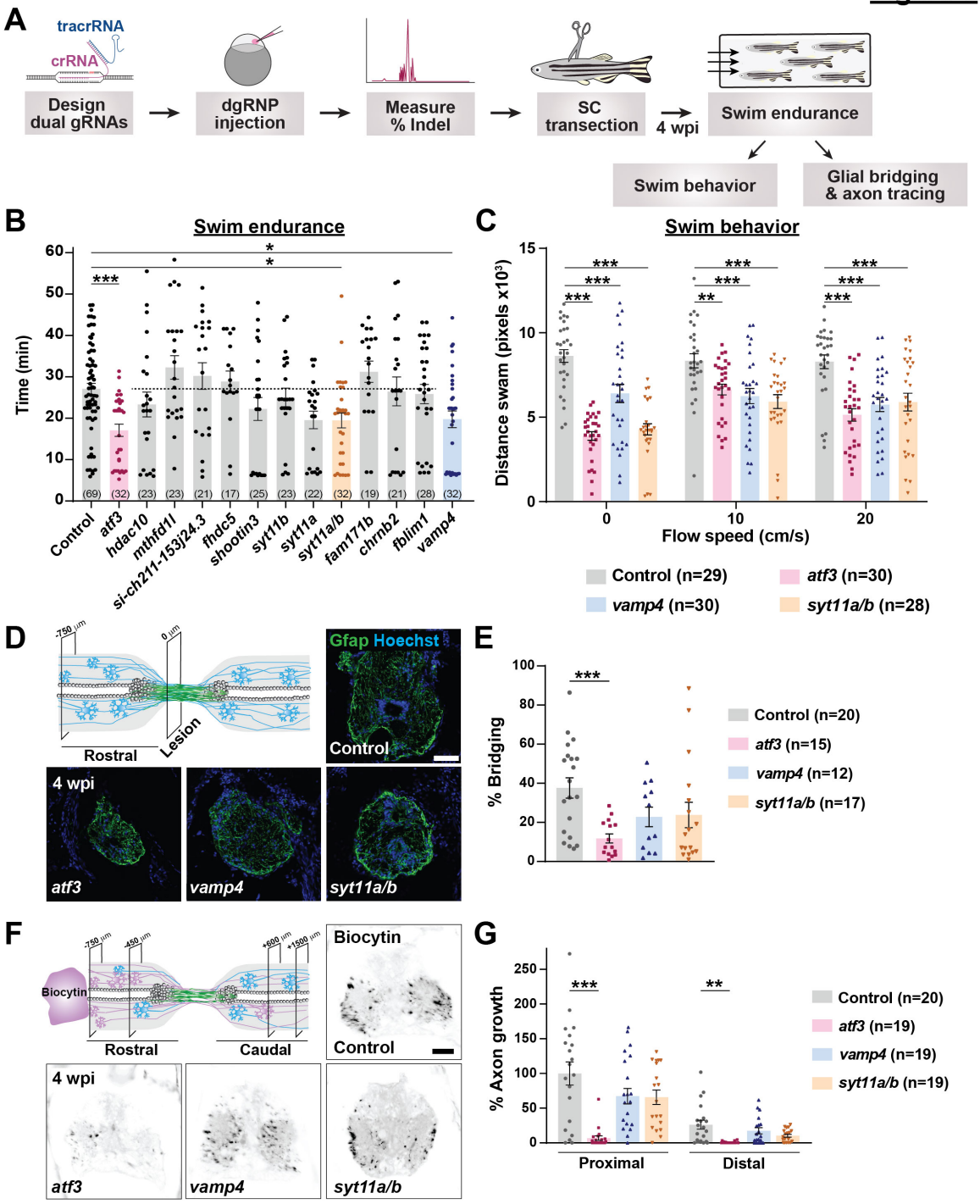
A
tracrRNA
crRNA
Design dual gRNAs
dgRNP injection
Measure % Indel
SC transection
4 wpi
Swim endurance
Swim behavior
Glial bridging & axon tracing
B
Swim endurance
Time (min)
Control
atf3
hdac10
mthfd1l
si-ch211-153j24.3
fhdc5
shootin3
syt11b
syt11a
syt11a/b
fam171b
chrnb2
fblim1
vamp4
C
Swim behavior
Distance swam (pixels x10³)
Flow speed (cm/s)
Control (n=29)
atf3 (n=30)
vamp4 (n=30)
syt11a/b (n=28)
D
Rostral
Lesion
Gfap Hoechst
Control
4 wpi
atf3
vamp4
syt11a/b
E
% Bridging
Control (n=20)
atf3 (n=15)
vamp4 (n=12)
syt11a/b (n=17)
F
Biocytin
Rostral
Caudal
Control
4 wpi
atf3
vamp4
syt11a/b
G
% Axon growth
Proximal
Distal
Control (n=20)
atf3 (n=19)
vamp4 (n=19)
syt11a/b (n=19)

Figure 8. CRISPR/Cas9 mutagenesis of N22 iNeuron marker genes in zebrafish. (A) Pipeline for CRISPR/Cas9 mutagenesis of N22 iNeuron marker genes for regeneration assessment. CRISPR/Cas9 dual-guide ribonucleic protein duplexes targeting iNeuron genes injected into one-cell zebrafish embryos. Mutagenesis efficiency was confirmed by capillary electrophoresis and animals with >90% mutagenesis were used for SCI. Swim endurance, swim behavior and histological regeneration assays were performed at 4 wpi. **(B)** Functional recovery in CRISPR/Cas9 targeted animals 4 wpi. For each group of targeted animals, uninjected siblings were subjected to SCI and swim endurance assays (ANOVA p-value <0.0001). Dots represent individual animals. The black dotted line marks average swim time in control animals. **(C)** Swim behavior assays in CRISPR/Cas9 targeted animals 4 wpi (ANOVA p-value <0.0001). Swim distance was tracked under water current velocities of 0, 10 and 20 cm/s. **(D,E)** Glial bridging in CRISPR/Cas9 targeted animals at 4 wpi. Representative immunohistochemistry shows the $Gfap^+$ bridge at the lesion site in *atf3, vamp4* and *syt11a/b* crispants relative to controls. Percent bridging represents the cross-sectional area of the glial bridge at the lesion site relative to the intact SC (ANOVA p-value: 0.0049). **(F,G)** Anterograde axon tracing in CRISPR/Cas9 targeted animals at 4 wpi. Biocytin axon tracer was applied rostrally and analyzed at 600 μm (proximal) (ANOVA p-value <0.0001) and 1500 μm (distal) (ANOVA p-value: 0.0006) caudal to the lesion. Representative traces of biocytin are shown at the proximal level. Axon regrowth was normalized to biocytin labeling in wild-type controls at the proximal level. Solid circles and polygons in the bar charts indicate individual animal and sample sizes are indicated in parentheses. Brown-Forsythe and Welch ANOVA test was performed in B, E and G with Dunnett's T3 multiple comparisons test performed across different time points with 95% CI. Two-way ANOVA with Dunnett's multiple comparisons test (95% CI) was performed in C. * p≤0.05, ** p ≤0.01, *** p≤0.001. Scale bars, 50 μm

REFERENCES

Ahlmann-Eltze, C. and Huber, W. (2021) 'glmGamPoi: fitting Gamma-Poisson generalized linear models on single cell count data', *Bioinformatics* 36(24): 5701-5702.

Anderson, M. A., O'Shea, T. M., Burda, J. E., Ao, Y., Barlatey, S. L., Bernstein, A. M., Kim, J. H., James, N. D., Rogers, A., Kato, B. et al. (2018) 'Required growth facilitators propel axon regeneration across complete spinal cord injury', *Nature* 561(7723): 396-400.

Baek, M., Menon, V., Jessell, T. M., Hantman, A. W. and Dasen, J. S. (2019) 'Molecular Logic of Spinocerebellar Tract Neuron Diversity and Connectivity', *Cell Rep* 27(9): 2620-2635 e4.

Bakken, T. E., Hodge, R. D., Miller, J. A., Yao, Z., Nguyen, T. N., Aevermann, B., Barkan, E., Bertagnolli, D., Casper, T., Dee, N. et al. (2018) 'Single-nucleus and single-cell transcriptomes compared in matched cortical cell types', *PLoS One* 13(12): e0209648.

Bakr, M., Jullie, D., Krapivkina, J., Paget-Blanc, V., Bouit, L., Petersen, J. D., Retailleau, N., Breillat, C., Herzog, E., Choquet, D. et al. (2021) 'The vSNAREs VAMP2 and VAMP4 control recycling and intracellular sorting of post-synaptic receptors in neuronal dendrites', *Cell Rep* 36(10): 109678.

Bartus, K., Burnside, E. R., Galino, J., James, N. D., Bennett, D. L. H. and Bradbury, E. J. (2019) 'ErbB receptor signaling directly controls oligodendrocyte progenitor cell transformation and spontaneous remyelination after spinal cord injury', *Glia* 67(6): 1036-1046.

Becht, E., McInnes, L., Healy, J., Dutertre, C. A., Kwok, I. W. H., Ng, L. G., Ginhoux, F. and Newell, E. W. (2018) 'Dimensionality reduction for visualizing single-cell data using UMAP', *Nat Biotechnol*.

Becker, C. G., Schweitzer, J., Feldner, J., Schachner, M. and Becker, T. (2004) 'Tenascin-R as a repellent guidance molecule for newly growing and regenerating optic axons in adult zebrafish', *Mol Cell Neurosci* 26(3): 376-89.

Bernhardt, R. R., Tongiorgi, E., Anzini, P. and Schachner, M. (1996) 'Increased expression of specific recognition molecules by retinal ganglion cells and by optic pathway glia accompanies the successful regeneration of retinal axons in adult zebrafish', *J Comp Neurol* 376(2): 253-64.

Bertels, H., Vicente-Ortiz, G., El Kanbi, K. and Takeoka, A. (2022) 'Neurotransmitter phenotype switching by spinal excitatory interneurons regulates locomotor recovery after spinal cord injury', *Nat Neurosci* 25(5): 617-629.

Bertuzzi, M., Chang, W. and Ampatzis, K. (2018) 'Adult spinal motoneurons change their neurotransmitter phenotype to control locomotion', *Proc Natl Acad Sci U S A* 115(42): E9926-E9933.

Brennan, F. H. and Popovich, P. G. (2018) 'Emerging targets for reprograming the immune response to promote repair and recovery of function after spinal cord injury', *Curr Opin Neurol* 31(3): 334-344.

Briona, L. K., Poulain, F. E., Mosimann, C. and Dorsky, R. I. (2015) 'Wnt/ss-catenin signaling is required for radial glial neurogenesis following spinal cord injury', *Dev Biol* 403(1): 15-21.

Burris, B., Jensen, N. and Mokalled, M. H. (2021) 'Assessment of Swim Endurance and Swim Behavior in Adult Zebrafish', *Journal of visualized experiments : JoVE*(177).

Busch, S. A. and Silver, J. (2007) 'The role of extracellular matrix in CNS regeneration', *Curr Opin Neurobiol* 17(1): 120-7.

Butler, A., Hoffman, P., Smibert, P., Papalexi, E. and Satija, R. (2018) 'Integrating single-cell transcriptomic data across different conditions, technologies, and species', *Nat Biotechnol* 36(5): 411-420.

Cavone, L., McCann, T., Drake, L. K., Aguzzi, E. A., Oprisoreanu, A. M., Pedersen, E., Sandi, S., Selvarajah, J., Tsarouchas, T. M., Wehner, D. et al. (2021) 'A unique macrophage subpopulation signals directly to progenitor cells to promote regenerative neurogenesis in the zebrafish spinal cord', *Developmental cell* 56(11): 1617-1630 e6.

Choi, H. M. T., Schwarzkopf, M., Fornace, M. E., Acharya, A., Artavanis, G., Stegmaier, J., Cunha, A. and Pierce, N. A. (2018) 'Third-generation in situ hybridization chain reaction: multiplexed, quantitative, sensitive, versatile, robust', *Development* 145(12).

Cohen, T., Gluzman-Poltorak, Z., Brodzky, A., Meytal, V., Sabo, E., Misselevich, I., Hassoun, M., Boss, J. H., Resnick, M., Shneyvas, D. et al. (2001) 'Neuroendocrine cells along the digestive tract express neuropilin-2', *Biochem Biophys Res Commun* 284(2): 395-403.

DePaul, M. A., Lin, C. Y., Silver, J. and Lee, Y. S. (2017) 'Combinatory repair strategy to promote axon regeneration and functional recovery after chronic spinal cord injury', *Sci Rep* 7(1): 9018.

Dias, T. B., Yang, Y. J., Ogai, K., Becker, T. and Becker, C. G. (2012) 'Notch signaling controls generation of motor neurons in the lesioned spinal cord of adult zebrafish', *J Neurosci* 32(9): 3245-52.

Ding, J., Adiconis, X., Simmons, S. K., Kowalczyk, M. S., Hession, C. C., Marjanovic, N. D., Hughes, T. K., Wadsworth, M. H., Burks, T., Nguyen, L. T. et al. (2020) 'Systematic comparison of single-cell and single-nucleus RNA-sequencing methods', *Nat Biotechnol* 38(6): 737-746.

Dudek, F. E. and Sutula, T. P. (2007) 'Epileptogenesis in the dentate gyrus: a critical perspective', *Prog Brain Res* 163: 755-73.

Durinck, S., Spellman, P. T., Birney, E. and Huber, W. (2009) 'Mapping identifiers for the integration of genomic datasets with the R/Bioconductor package biomaRt', *Nat Protoc* 4(8): 1184-91.

Falk, J., Bechara, A., Fiore, R., Nawabi, H., Zhou, H., Hoyo-Becerra, C., Bozon, M., Rougon, G., Grumet, M., Puschel, A. W. et al. (2005) 'Dual functional activity of semaphorin 3B is required for positioning the anterior commissure', *Neuron* 48(1): 63-75.

Ferrario, J. E., Baskaran, P., Clark, C., Hendry, A., Lerner, O., Hintze, M., Allen, J., Chilton, J. K. and Guthrie, S. (2012) 'Axon guidance in the developing ocular motor system and Duane retraction syndrome depends on Semaphorin signaling via alpha2-chimaerin', *Proc Natl Acad Sci U S A* 109(36): 14669-74.

Fouad, K., Popovich, P. G., Kopp, M. A. and Schwab, J. M. (2021) 'The neuroanatomical-functional paradox in spinal cord injury', *Nat Rev Neurol* 17(1): 53-62.

Gao, R. and Penzes, P. (2015) 'Common mechanisms of excitatory and inhibitory imbalance in schizophrenia and autism spectrum disorders', *Curr Mol Med* 15(2): 146-67.

Gey, M., Wanner, R., Schilling, C., Pedro, M. T., Sinske, D. and Knoll, B. (2016) 'Atf3 mutant mice show reduced axon regeneration and impaired regeneration-associated gene induction after peripheral nerve injury', *Open Biol* 6(8).

Goldshmit, Y., Sztal, T. E., Jusuf, P. R., Hall, T. E., Nguyen-Chi, M. and Currie, P. D. (2012) 'Fgf-dependent glial cell bridges facilitate spinal cord regeneration in zebrafish', *J Neurosci* 32(22): 7477-92.

Guillemot, F. (2007) 'Spatial and temporal specification of neural fates by transcription factor codes', *Development* 134(21): 3771-80.

Gulati, G. S., Sikandar, S. S., Wesche, D. J., Manjunath, A., Bharadwaj, A., Berger, M. J., Ilagan, F., Kuo, A. H., Hsieh, R. W., Cai, S. et al. (2020) 'Single-cell transcriptional diversity is a hallmark of developmental potential', *Science* 367(6476): 405-411.

Haenisch, C., Diekmann, H., Klinger, M., Gennarini, G., Kuwada, J. Y. and Stuermer, C. A. (2005) 'The neuronal growth and regeneration associated Cntn1 (F3/F11/Contactin) gene is duplicated in fish: expression during development and retinal axon regeneration', *Mol Cell Neurosci* 28(2): 361-74.

Hafemeister, C. and Satija, R. (2019) 'Normalization and variance stabilization of single-cell RNA-seq data using regularized negative binomial regression', *Genome Biol* 20(1): 296.

Haghverdi, L., Lun, A. T. L., Morgan, M. D. and Marioni, J. C. (2018) 'Batch effects in single-cell RNA-sequencing data are corrected by matching mutual nearest neighbors', *Nat Biotechnol* 36(5): 421-427.

Haring, M., Zeisel, A., Hochgerner, H., Rinwa, P., Jakobsson, J. E. T., Lonnerberg, P., La Manno, G., Sharma, N., Borgius, L., Kiehn, O. et al. (2018) 'Neuronal atlas of the dorsal horn defines its architecture and links sensory input to transcriptional cell types', *Nat Neurosci* 21(6): 869-880.

Hayashi, M., Hinckley, C. A., Driscoll, S. P., Moore, N. J., Levine, A. J., Hilde, K. L., Sharma, K. and Pfaff, S. L. (2018) 'Graded Arrays of Spinal and Supraspinal V2a Interneuron Subtypes Underlie Forelimb and Hindlimb Motor Control', *Neuron* 97(4): 869-884 e5.

He, Z. and Jin, Y. (2016) 'Intrinsic Control of Axon Regeneration', *Neuron* 90(3): 437-51.

Hernandez-Miranda, L. R., Muller, T. and Birchmeier, C. (2017) 'The dorsal spinal cord and hindbrain: From developmental mechanisms to functional circuits', *Dev Biol* 432(1): 34-42.

Hilton, B. J., Husch, A., Schaffran, B., Lin, T. C., Burnside, E. R., Dupraz, S., Schelski, M., Kim, J., Muller, J. A., Schoch, S. et al. (2022) 'An active vesicle priming machinery suppresses axon regeneration upon adult CNS injury', *Neuron* 110(1): 51-69 e7.

Hou, J., Bi, H., Ge, Q., Teng, H., Wan, G., Yu, B., Jiang, Q. and Gu, X. (2022) 'Heterogeneity analysis of astrocytes following spinal cord injury at single-cell resolution', *FASEB J* 36(8): e22442.

Huang, C. X., Zhao, Y., Mao, J., Wang, Z., Xu, L., Cheng, J., Guan, N. N. and Song, J. (2021) 'An injury-induced serotonergic neuron subpopulation contributes to axon regrowth and function restoration after spinal cord injury in zebrafish', *Nat Commun* 12(1): 7093.

Ilicic, T., Kim, J. K., Kolodziejczyk, A. A., Bagger, F. O., McCarthy, D. J., Marioni, J. C. and Teichmann, S. A. (2016) 'Classification of low quality cells from single-cell RNA-seq data', *Genome Biol* 17: 29.

Isaacson, J. S. and Scanziani, M. (2011) 'How inhibition shapes cortical activity', *Neuron* 72(2): 231-43.

Jankowski, M. P., McIlwrath, S. L., Jing, X., Cornuet, P. K., Salerno, K. M., Koerber, H. R. and Albers, K. M. (2009) 'Sox11 transcription factor modulates peripheral nerve regeneration in adult mice', *Brain Res* 1256: 43-54.

Jin, S., Guerrero-Juarez, C. F., Zhang, L., Chang, I., Ramos, R., Kuan, C. H., Myung, P., Plikus, M. V. and Nie, Q. (2021) 'Inference and analysis of cell-cell communication using CellChat', *Nat Commun* 12(1): 1088.

Jing, X., Wang, T., Huang, S., Glorioso, J. C. and Albers, K. M. (2012) 'The transcription factor Sox11 promotes nerve regeneration through activation of the regeneration-associated gene Sprr1a', *Exp Neurol* 233(1): 221-32.

Jung, M., Petrausch, B. and Stuermer, C. A. (1997) 'Axon-regenerating retinal ganglion cells in adult rats synthesize the cell adhesion molecule L1 but not TAG-1 or SC-1', *Mol Cell Neurosci* 9(2): 116-31.

Klatt Shaw, D. and Mokalled, M. H. (2021) 'Efficient CRISPR/Cas9 mutagenesis for neurobehavioral screening in adult zebrafish', *G3 (Bethesda)* 11(8).

Klatt Shaw, D., Saraswathy, V. M., Zhou, L., McAdow, A. R., Burris, B., Butka, E., Morris, S. A., Dietmann, S. and Mokalled, M. H. (2021) 'Localized EMT reprograms glial progenitors to promote spinal cord repair', *Developmental cell* 56(5): 613-626 e7.

Kole, C., Brommer, B., Nakaya, N., Sengupta, M., Bonet-Ponce, L., Zhao, T., Wang, C., Li, W., He, Z. and Tomarev, S. (2020) 'Activating Transcription Factor 3 (ATF3) Protects Retinal Ganglion Cells and Promotes Functional Preservation After Optic Nerve Crush', *Invest Ophthalmol Vis Sci* 61(2): 31.

Kuscha, V., Frazer, S. L., Dias, T. B., Hibi, M., Becker, T. and Becker, C. G. (2012) 'Lesion-induced generation of interneuron cell types in specific dorsoventral domains in the spinal cord of adult zebrafish', *J Comp Neurol* 520(16): 3604-16.

Lacar, B., Linker, S. B., Jaeger, B. N., Krishnaswami, S. R., Barron, J. J., Kelder, M. J. E., Parylak, S. L., Paquola, A. C. M., Venepally, P., Novotny, M. et al. (2016) 'Nuclear RNA-seq of single neurons reveals molecular signatures of activation', *Nat Commun* 7: 11022.

Lake, B. B., Codeluppi, S., Yung, Y. C., Gao, D., Chun, J., Kharchenko, P. V., Linnarsson, S. and Zhang, K. (2017) 'A comparative strategy for single-nucleus and single-cell transcriptomes confirms accuracy in predicted cell-type expression from nuclear RNA', *Sci Rep* 7(1): 6031.

Lange, M., Bergen, V., Klein, M., Setty, M., Reuter, B., Bakhti, M., Lickert, H., Ansari, M., Schniering, J., Schiller, H. B. et al. (2022) 'CellRank for directed single-cell fate mapping', *Nat Methods* 19(2): 159-170.

Lawson, N. D., Li, R., Shin, M., Grosse, A., Yukselen, O., Stone, O. A., Kucukural, A. and Zhu, L. (2020) 'An improved zebrafish transcriptome annotation for sensitive and comprehensive detection of cell type-specific genes', *Elife* 9.

Levine, J. H., Simonds, E. F., Bendall, S. C., Davis, K. L., Amir el, A. D., Tadmor, M. D., Litvin, O., Fienberg, H. G., Jager, A., Zunder, E. R. et al. (2015) 'Data-Driven Phenotypic Dissection of AML Reveals Progenitor-like Cells that Correlate with Prognosis', *Cell* 162(1): 184-97.

Li, W. R., Wang, Y. L., Li, C., Gao, P., Zhang, F. F., Hu, M., Li, J. C., Zhang, S., Li, R. and Zhang, C. X. (2021) 'Synaptotagmin-11 inhibits spontaneous neurotransmission through vti1a', *J Neurochem* 159(4): 729-741.

Lin, P. Y., Chanaday, N. L., Horvath, P. M., Ramirez, D. M. O., Monteggia, L. M. and Kavalali, E. T. (2020) 'VAMP4 Maintains a Ca(2+)-Sensitive Pool of Spontaneously Recycling Synaptic Vesicles', *J Neurosci* 40(28): 5389-5401.

Lu, D. C., Niu, T. and Alaynick, W. A. (2015) 'Molecular and cellular development of spinal cord locomotor circuitry', *Front Mol Neurosci* 8: 25.

Matson, K. J. E., Russ, D. E., Kathe, C., Hua, I., Maric, D., Ding, Y., Krynitsky, J., Pursley, R., Sathyamurthy, A., Squair, J. W. et al. (2022) 'Single cell atlas of spinal cord injury in mice reveals a pro-regenerative signature in spinocerebellar neurons', *Nat Commun* 13(1): 5628.

Matson, K. J. E., Sathyamurthy, A., Johnson, K. R., Kelly, M. C., Kelley, M. W. and Levine, A. J. (2018) 'Isolation of Adult Spinal Cord Nuclei for Massively Parallel Single-nucleus RNA Sequencing', *Journal of visualized experiments : JoVE*(140).

Mikami, T., Yasunaga, D. and Kitagawa, H. (2009) 'Contactin-1 is a functional receptor for neuroregulatory chondroitin sulfate-E', *J Biol Chem* 284(7): 4494-9.

Milich, L. M., Choi, J. S., Ryan, C., Cerqueira, S. R., Benavides, S., Yahn, S. L., Tsoulfas, P. and Lee, J. K. (2021) 'Single-cell analysis of the cellular heterogeneity and interactions in the injured mouse spinal cord', *J Exp Med* 218(8).

Milich, L. M., Ryan, C. B. and Lee, J. K. (2019) 'The origin, fate, and contribution of macrophages to spinal cord injury pathology', *Acta Neuropathol* 137(5): 785-797.

Mokalled, M. H., Patra, C., Dickson, A. L., Endo, T., Stainier, D. Y. and Poss, K. D. (2016) 'Injury-induced ctgfa directs glial bridging and spinal cord regeneration in zebrafish', *Science* 354(6312): 630-634.

Nakamura, Y., Ueno, M., Niehaus, J. K., Lang, R. A., Zheng, Y. and Yoshida, Y. (2021) 'Modulation of Both Intrinsic and Extrinsic Factors Additively Promotes Rewiring of Corticospinal Circuits after Spinal Cord Injury', *J Neurosci* 41(50): 10247-10260.

Nicholson-Fish, J. C., Kokotos, A. C., Gillingwater, T. H., Smillie, K. J. and Cousin, M. A. (2015) 'VAMP4 Is an Essential Cargo Molecule for Activity-Dependent Bulk Endocytosis', *Neuron* 88(5): 973-984.

Park, K. K., Liu, K., Hu, Y., Smith, P. D., Wang, C., Cai, B., Xu, B., Connolly, L., Kramvis, I., Sahin, M. et al. (2008) 'Promoting axon regeneration in the adult CNS by modulation of the PTEN/mTOR pathway', *Science* 322(5903): 963-6.

R Core Team (2018) R: A language and environment for statistical computing, https://www.R-project.org/.

Reimer, M. M., Kuscha, V., Wyatt, C., Sorensen, I., Frank, R. E., Knuwer, M., Becker, T. and Becker, C. G. (2009) 'Sonic hedgehog is a polarized signal for motor neuron regeneration in adult zebrafish', *J Neurosci* 29(48): 15073-82.

Reimer, M. M., Sorensen, I., Kuscha, V., Frank, R. E., Liu, C., Becker, C. G. and Becker, T. (2008) 'Motor neuron regeneration in adult zebrafish', *The Journal of neuroscience : the official journal of the Society for Neuroscience* 28(34): 8510-6.

Ren, Y., Ao, Y., O'Shea, T. M., Burda, J. E., Bernstein, A. M., Brumm, A. J., Muthusamy, N., Ghashghaei, H. T., Carmichael, S. T., Cheng, L. et al. (2017) 'Ependymal cell contribution to scar formation after spinal cord injury is minimal, local and dependent on direct ependymal injury', *Sci Rep* 7: 41122.

Rodrigo Albors, A., Singer, G. A., Llorens-Bobadilla, E., Frisen, J., May, A. P., Ponting, C. P. and Storey, K. G. (2023) 'An ependymal cell census identifies heterogeneous and ongoing cell maturation in the adult mouse spinal cord that changes dynamically on injury', *Developmental cell* 58(3): 239-255 e10.

Rosenberg, A. B., Roco, C. M., Muscat, R. A., Kuchina, A., Sample, P., Yao, Z., Graybuck, L. T., Peeler, D. J., Mukherjee, S., Chen, W. et al. (2018) 'Single-cell profiling of the developing mouse brain and spinal cord with split-pool barcoding', *Science* 360(6385): 176-182.

Rossum, G.V. and Drake, F.L. (2009) Python 3 Reference Manual.

Rougeot, J., Torraca, V., Zakrzewska, A., Kanwal, Z., Jansen, H. J., Sommer, F., Spaink, H. P. and Meijer, A. H. (2019) 'RNAseq Profiling of Leukocyte Populations in Zebrafish Larvae Reveals a cxcl11 Chemokine Gene as a Marker of Macrophage Polarization During Mycobacterial Infection', *Front Immunol* 10: 832.

Salic, A. and Mitchison, T. J. (2008) 'A chemical method for fast and sensitive detection of DNA synthesis in vivo', *Proc Natl Acad Sci U S A* 105(7): 2415-20.

Saraswathy, V. M., Zhou, L., McAdow, A. R., Burris, B., Dogra, D., Reischauer, S. and Mokalled, M. H. (2022) 'Myostatin is a negative regulator of adult neurogenesis after spinal cord injury in zebrafish', *Cell Rep* 41(8): 111705.

Sathyamurthy, A., Johnson, K. R., Matson, K. J. E., Dobrott, C. I., Li, L., Ryba, A. R., Bergman, T. B., Kelly, M. C., Kelley, M. W. and Levine, A. J. (2018) 'Massively Parallel Single Nucleus Transcriptional Profiling Defines Spinal Cord Neurons and Their Activity during Behavior', *Cell Rep* 22(8): 2216-2225.

Satou, C., Kimura, Y., Hirata, H., Suster, M. L., Kawakami, K. and Higashijima, S. (2013) 'Transgenic tools to characterize neuronal properties of discrete populations of zebrafish neurons', *Development* 140(18): 3927-31.

Scott, K., O'Rourke, R., Winkler, C. C., Kearns, C. A. and Appel, B. (2021) 'Temporal single-cell transcriptomes of zebrafish spinal cord pMN progenitors reveal distinct neuronal and glial progenitor populations', *Dev Biol* 479: 37-50.

Shah, P. T., Stratton, J. A., Stykel, M. G., Abbasi, S., Sharma, S., Mayr, K. A., Koblinger, K., Whelan, P. J. and Biernaskie, J. (2018) 'Single-Cell Transcriptomics and Fate Mapping of Ependymal Cells Reveals an Absence of Neural Stem Cell Function', *Cell* 173(4): 1045-1057 e9.

Shimojo, M., Madara, J., Pankow, S., Liu, X., Yates, J., 3rd, Sudhof, T. C. and Maximov, A. (2019) 'Synaptotagmin-11 mediates a vesicle trafficking pathway that is essential for development and synaptic plasticity', *Genes Dev* 33(5-6): 365-376.

Sofroniew, M. V. (2018) 'Dissecting spinal cord regeneration', *Nature* 557(7705): 343-350.

Stassen, S. V., Yip, G. G. K., Wong, K. K. Y., Ho, J. W. K. and Tsia, K. K. (2021) 'Generalized and scalable trajectory inference in single-cell omics data with VIA', *Nat Commun* 12(1): 5528.

Stuart, T., Butler, A., Hoffman, P., Hafemeister, C., Papalexi, E., Mauck, W. M., 3rd, Hao, Y., Stoeckius, M., Smibert, P. and Satija, R. (2019) 'Comprehensive Integration of Single-Cell Data', *Cell* 177(7): 1888-1902 e21.

Tambalo, M., Mitter, R. and Wilkinson, D. G. (2020) 'A single cell transcriptome atlas of the developing zebrafish hindbrain', *Development* 147(6).

Tang, Q., Iyer, S., Lobbardi, R., Moore, J. C., Chen, H., Lareau, C., Hebert, C., Shaw, M. L., Neftel, C., Suva, M. L. et al. (2017) 'Dissecting hematopoietic and renal cell heterogeneity in adult zebrafish at single-cell resolution using RNA sequencing', *J Exp Med* 214(10): 2875-2887.

Tran, A. P., Warren, P. M. and Silver, J. (2022) 'New insights into glial scar formation after spinal cord injury', *Cell Tissue Res* 387(3): 319-336.

van den Brink, S. C., Sage, F., Vertesy, A., Spanjaard, B., Peterson-Maduro, J., Baron, C. S., Robin, C. and van Oudenaarden, A. (2017) 'Single-cell sequencing reveals dissociation-induced gene expression in tissue subpopulations', *Nat Methods* 14(10): 935-936.

Vandestadt, C., Vanwalleghem, G. C., Khabooshan, M. A., Douek, A. M., Castillo, H. A., Li, M., Schulze, K., Don, E., Stamatis, S. A., Ratnadiwakara, M. et al. (2021) 'RNA-induced inflammation and migration of precursor neurons initiates neuronal circuit regeneration in zebrafish', *Developmental cell* 56(16): 2364-2380 e8.

Walsh, F. S. and Doherty, P. (1996) 'Cell adhesion molecules and neuronal regeneration', *Curr Opin Cell Biol* 8(5): 707-13.

Wang, C., Wang, Y., Hu, M., Chai, Z., Wu, Q., Huang, R., Han, W., Zhang, C. X. and Zhou, Z. (2016) 'Synaptotagmin-11 inhibits clathrin-mediated and bulk endocytosis', *EMBO Rep* 17(1): 47-63.

Wang, L. F., Huang, S. B., Zhao, H. D., Liu, C. J., Yao, L. and Shen, Y. Q. (2017) 'Activating transcription factor 3 promotes spinal cord regeneration of adult zebrafish', *Biochem Biophys Res Commun* 488(3): 522-527.

Wang, Z., Reynolds, A., Kirry, A., Nienhaus, C. and Blackmore, M. G. (2015) 'Overexpression of Sox11 promotes corticospinal tract regeneration after spinal injury while interfering with functional recovery', *J Neurosci* 35(7): 3139-45.

Wu, H., Kirita, Y., Donnelly, E. L. and Humphreys, B. D. (2019) 'Advantages of Single-Nucleus over Single-Cell RNA Sequencing of Adult Kidney: Rare Cell Types and Novel Cell States Revealed in Fibrosis', *J Am Soc Nephrol* 30(1): 23-32.

Xu, C. and Su, Z. (2015) 'Identification of cell types from single-cell transcriptomes using a novel clustering method', *Bioinformatics* 31(12): 1974-80.

Yadav, A., Matson, K. J. E., Li, L., Hua, I., Petrescu, J., Kang, K., Alkaslasi, M. R., Lee, D. I., Hasan, S., Galuta, A. et al. (2023) 'A cellular taxonomy of the adult human spinal cord', *Neuron* 111(3): 328-344 e7.

Yao, C., Cao, Y., Wang, D., Lv, Y., Liu, Y., Gu, X., Wang, Y., Wang, X. and Yu, B. (2022) 'Single-cell sequencing reveals microglia induced angiogenesis by specific subsets of endothelial cells following spinal cord injury', *FASEB J* 36(7): e22393.

Zappia, L. and Oshlack, A. (2018) 'Clustering trees: a visualization for evaluating clusterings at multiple resolutions', *Gigascience* 7(7).

Zeisel, A., Hochgerner, H., Lonnerberg, P., Johnsson, A., Memic, F., van der Zwan, J., Haring, M., Braun, E., Borm, L. E., La Manno, G. et al. (2018) 'Molecular Architecture of the Mouse Nervous System', *Cell* 174(4): 999-1014 e22.

Zhang, H., Fang, X., Huang, D., Luo, Q., Zheng, M., Wang, K., Cao, L. and Yin, Z. (2018) 'Erythropoietin signaling increases neurogenesis and oligodendrogenesis of endogenous neural stem cells following spinal cord injury both in vivo and in vitro', *Mol Med Rep* 17(1): 264-272.

Zhang, Y., Chen, K., Sloan, S. A., Bennett, M. L., Scholze, A. R., O'Keeffe, S., Phatnani, H. P., Guarnieri, P., Caneda, C., Ruderisch, N. et al. (2014) 'An RNA-sequencing transcriptome and splicing database of glia, neurons, and vascular cells of the cerebral cortex', *J Neurosci* 34(36): 11929-47.

Zhang, Y., Yeh, J., Richardson, P. M. and Bo, X. (2008) 'Cell adhesion molecules of the immunoglobulin superfamily in axonal regeneration and neural repair', *Restor Neurol Neurosci* 26(2-3): 81-96.

Zhou, Y., Zhou, B., Pache, L., Chang, M., Khodabakhshi, A. H., Tanaseichuk, O., Benner, C. and Chanda, S. K. (2019) 'Metascape provides a biologist-oriented resource for the analysis of systems-level datasets', *Nat Commun* 10(1): 1523.

Zhu, Y., Soderblom, C., Trojanowsky, M., Lee, D. H. and Lee, J. K. (2015) 'Fibronectin Matrix Assembly after Spinal Cord Injury', *J Neurotrauma* 32(15): 1158-67.